https://dx.doi.org/10.1016/j.actamat.2022.117763

$L1_2$-strengthened multicomponent Co-Al-Nb-based alloys with high strength and matrix-confined stacking-fault-mediated plasticity

B.X. Cao[1, 2], W.-W. Xu,[3] C.Y. Yu[4], S.W. Wu[1], H.J. Kong[5], Z.Y. Ding[6, 7], T.L. Zhang[1, 2], J.H. Luan[1], B. Xiao[5], Z.B. Jiao[7], Y. Liu[8], T. Yang[1, 2*], C.T. Liu[1, 2, 5*]

[1] *Department of Materials Science and Engineering, City University of Hong Kong, Hong Kong, China*

[2] *Hong Kong Institute for Advanced Study, City University of Hong Kong, Hong Kong, China*

[3] *School of Aerospace Engineering, Xiamen University, Xiamen 361005, China*

[4] *College of Physics and Optoelectronic Engineering, Shenzhen University, Shenzhen 518060, China*

[5] *Department of Mechanical Engineering, City University of Hong Kong, Hong Kong, China*

[6] *School of Materials and Chemistry, University of Shanghai for Science and Technology, Shanghai 200093, China*

[7] *Department of Mechanical Engineering, The Hong Kong Polytechnic University, Hong Kong, China*

[8] *The State Key Laboratory of Powder Metallurgy, Central South University, Changsha 410083, China*

[*] *Corresponding authors: taoyang6-c@my.cityu.edu.hk (T. Yang); chainliu@cityu.edu.hk (C.T. Liu)*

Abstract

This study presents the alloy development of a new class of $L1_2$-strengthened Co-Al-Nb-based alloys with high γ′-solvus temperatures together with superb strengths at both ambient and elevated temperatures. The $L1_2$-Co_3(Al, Nb) phase was found to be in equilibrium with the γ-Co matrix and the B2-CoAl phase in ternary Co-10Al-3Nb alloys after isothermal aging at 700 °C; however, it transformed into the Laves phase as the aging temperature increased to 800 °C. Alloying addition of Ni helped to suppress the B2 phase formation, resulting in a clean γ-γ′ dual-phase microstructure. Ti and Ta elements further stabilized the $L1_2$ structure and increased the γ′-solvus temperature to 1150 °C without inducing the formation of other deleterious intermetallic phases. The newly developed Co-Al-Nb-Ni-Ti-Ta multicomponent Co-rich alloy has demonstrated outstanding yield strengths at both ambient and elevated temperatures, reaching 1023 ± 27 MPa at 25 °C and 897 ± 53 MPa at 700 °C, respectively. Furthermore, detailed electron microscopy analyses uncovered unique deformation substructures, in which plasticity is predominantly carried out via nanoscale matrix-channel-confined stacking faults. As determined by the first-principle calculations, the absence of particle shearing upon deformation at ambient temperature is ascribed to the ultrahigh planar fault energies of the multicomponent γ′ precipitates. High-density superlattice-stacking-fault shearing and their interactions are responsible for the yield anomaly at 700 °C. These findings not only provide the fundamental understanding of the deformation behavior of the $L1_2$-strengthened alloys, but also demonstrate the great potential for developing next-generation high-temperature structural materials based on the multicomponent Co-rich alloy systems.

Keywords*:* Phase stability; Mechanical properties; High-temperature strength; Cobalt-based alloys; Deformation mechanisms

1

1. Introduction

The discovery of γ′-Co_3(Al, W) precipitates with the $L1_2$ ordering in Co-Al-W ternary alloys provides new opportunities for developing next-generation high-temperature structural materials within Co-rich alloy systems [1]. Utilizing ordered precipitation for strengthening requires the strengtheners to be thermodynamically stable at operating temperatures. However, it was reported that the $L1_2$-Co_3(Al, W) phase is metastable at elevated temperatures, which decomposed into the B2-CoAl phase and $D0_{19}$-Co_3W phase upon long-term annealing at 900 °C [2-4]. For comparison purposes, the $L1_2$-type Ni_3(Al, Ti) precipitates remain stable up to 1100 °C among advanced Ni-based superalloys [5]. Moreover, an optimized microstructure consisting of the "γ-matrix + γ′-precipitates" dual phases is preferred without the formation of other deleterious intermetallic phases [6]. However, most quaternary alloying additions to the ternary Co-Al-W alloy tend to induce the formation of brittle intermetallic phases [7]. These undesired intermetallic phases might cause severe embrittlement and catastrophic brittle fractures during tensile deformation. Additionally, such intermetallic phases can also deplete refractory elements from the matrix, diminishing the effectiveness of solid-solution strengthening [8-10]. The coarsening rate of the γ′ precipitates would also get accelerated by refractory element consumptions. Inhibiting the overall γ′ coarsening is beneficial for the development of high-temperature structural materials with high thermal stability and long service lifetimes [11, 12]. Therefore, in this study we focus on the stabilization of the γ′ precipitates without degrading the γ-γ′ dual-phase microstructure within the Co-based alloy systems.

The $L1_2$-type Co_3Al phase was once discovered in Co-Al binary alloys as a metastable phase [13]. Still, upon aging at 600 °C, the Co-Al binary alloy was more prone to form the discontinuous precipitation of the B2-type CoAl phase in equilibrium with the γ-Co matrix [13]. Noteworthy is that certain transition elements from the VB and VIB groups (Mo, W, Ta, V)

were reported to stabilize the $L1_2$-Co_3Al phase by forming the ternary $L1_2$-$Co_3(Al, X)$ (X = Mo, W, Ta, V) phases. Density functional theory (DFT) calculations also confirmed that these transition elements are expected to promote $L1_2$ ordering among Co-Al-based alloys [14]. Taking the Co-Al-W ternary alloy as an example, first-principle calculations revealed that the $Co_3(Al, W)$ phase is not an equilibrium phase with respect to the B2-type CoAl and $D0_{19}$-Co_3W phases at 0 K [15]. However, the stability of the $Co_3(Al, W)$ phase benefited from the entropy contributions at non-zero temperatures [15]. Moreover, the excess Co occupying the B sublattice site in the $L1_2$-type A_3B intermetallic phase, instead of keeping a strict stoichiometric ratio (3:1), also enhance the stability of the $Co_3(Al, W)$ phase [3]. Therefore, the Co-Al-X system (X is a transition element from the VB or VIB groups) is promising for designing novel $L1_2$-strengthened Co-based alloys. Noticeably, as a transition element from the VB group, niobium (Nb) is expected to promote $L1_2$ ordering in the Co-based alloys along this line of thought. In fact, the feasibility of forming the $L1_2$-type $Co_3(Al, Nb)$ phase has been reported in a recent DFT study [16]. Another earlier work also indicated that the $L1_2$-$Co_3(Al, Nb)$ intermetallic compound was more stable than the $D0_{19}$-type intermetallic phase [17]. Apart from these theoretical calculations, experimental studies also revealed that Nb is partitioned to the γ′ precipitates and acted as the γ′ stabilizer among Co-based alloys [18, 19]. It is noteworthy that the $L1_2$-structured Co_3Nb has been previously reported in Co-Nb binary alloy, but only as a metastable phase that formed only at the early stage of heat treatment. The metastable γ′-Co_3Nb phase eventually transformed into the Nb-rich Laves phase with a prolonged aging time [20]. Collectively, these preliminary results suggest the promising potential for forming ordered $L1_2$ precipitates among the Co-Al-Nb alloy system.

In addition to the phase stability, the mass density should also be well taken into considerations in evaluating their potential for engineering applications. Due to the fact that a large proportion of the high-density tungsten is required for the stabilization of the $L1_2$ phase

in the Co-Al-W-based alloys, their mass densities are generally too high (e.g., 9.82 g cm^{-3} for the Co-9Al-9.8W alloy) [1, 7]. As a result, the development of W-free Co-based alloys with a reduced mass density has received a priority attention recently [19]. Alternatively, the mass density of Nb is only 8.57 g cm^{-3}, which is less than half of that of W (19.3 g cm^{-3}). Therefore, designinging the novel W-free Co-Al-Nb-based alloys can effectively reduce the mass density, which sheds light on a potential promising path for developing new structural materials with high specific strengths.

In this study, we systematically investigated the potential of utilizing the ordered $L1_2$ precipitates for strengthening within the multicomponent Co-Al-Nb-based alloys. The phase equilibria, γ′-solvus temperature, and microstructural stability of the ternary Co-Al-Nb alloy have been carefully investigated for the first time. More importantly, the innovative design of the $L1_2$-strengthened Co-Al-Nb-based alloys with high strengths at both ambient and elevated temperatures was also carefully addressed in the present study. Deformation behaviors and associated deformation substructures consisting of nanoscale matrix-channel-confined stacking faults were also unveiled upon plastic deformation at ambient temperature. High-density superlattice-stacking-fault-based particle shearing and their interactions are responsible for the yield anomaly at 700 °C. These findings not only promote the fundamental understanding of the deformation behaviors of the $L1_2$-strengthened alloys, but also demonstrate the potential for developing next-generation high-temperature structural materials within the multicomponent Co-rich alloy systems.

2. Experimental procedures

2.1. Materials preparation

Alloy ingots based on the Co-Al-Nb system were prepared by arc melting high-purity raw metals (99.9 wt.%) in a Ti-gettered Ar atmosphere. They were flipped and remelted no less

than five times to ensure the compositional homogeneity, and then drop casted into a copper mold with a size of 5 × 12 × 100 mm^3. The as-cast samples were first homogenized at 1200 °C for 2 h and then cold-rolled with ~50% reduction in thickness, followed by recrystallization at 1200 °C for 2 min. Subsequently, the alloy samples were aged at 700/800 °C for precipitation growth. Due to the sluggish diffusion kinetics and the resultant small particle size, some specimens were annealed directly after cold-rolling to accelerate atomic diffusion and obtain a coarsened microstructure. Air cooling was applied after each heat treatment step to avoid potential intergranular cracking caused by water quenching.

2.2. Materials characterizations

Microstructural characterizations were carried out by scanning electron microscopy (SEM, Quanta 450), transmission electron microscopy (TEM, JEOL 2100F), X-ray diffractometer (XRD, Rigaku), and differential scanning calorimeter (DSC, NETZSCH 404C). For SEM observation, the samples were first mechanically grounded by SiC papers and then electro-polished using an electrolyte of 20 vol.% nitric acid and 80 vol.% ethanol at 20 V/-40 °C. For TEM analyses, specimens were mechanically grounded to a thickness of 50 μm and then punched into discs with a diameter of 3 mm, followed by ion-milling via a precision ion polishing system (Gatan 695). The X-ray diffraction data were collected from 20° to 100° with a step size of 0.02° and a speed of 2° per minute. The mismatch between the γ and γ′ phases was calculated by peak deconvolutions using the pseudo-Voigt function.

The atomic-scale compositional analysis was carried out by atom probe tomography (APT, CAMECA LEAP 5000 XR). The APT specimen was first fabricated by lift-out procedures and then annular-milled using a focused-ion-beam/scanning electron microscope (FIB/SEM, FEI, Scios). The APT measurement was conducted at 70 K under the voltage mode with a pulse frequency of 200 kHz, a detection rate of 0.2% atom per pulse, and a pulse fraction

of 20%. Image Visualization and Analysis Software package (IVAS 3.8.2) was used for data analyses and reconstructions.

2.3. Mechanical tests

Cylindrical specimens with a diameter of 5 mm and a length of 10 mm were sectioned from the aged samples by electro-discharge machining. Compression tests were conducted at both ambient and elevated temperatures under a strain rate of 10^{-3} s^{-1} in air. To avoid the temperature fluctuation inside the furnace, three thermocouples were used to monitor the temperature inside the furnace to ensure the equilibrium temperature was reached during compression tests.

2.4. Theoretical calculations

Energies of the $L1_2$-Co_3(Al, Nb) phases with various Nb concentrations were examined by the first-principles calculations via the Projector augmented wave (PAW) [21] pseudopotential approach. They were carried out by employing the Vienna ab initio Simulation Package [22], and the generalized gradient approximation (GGA) refined by Perdew, Burke, and Ernzerhof (PBE) [23] was applied to describe the electronic exchange and correlation. A three-dimensional supercell with 3 × 3 × 3 unit cells was constructed for each composition to determine the total energy. The energy cutoff was set to 500 eV, and 1 × 1 × 1 Γ-centered Monkhorst-Pack grids were adopted for Brillouin zone integrations [24]. All the calculations were spin-polarized, equilibrium cell volumes and all atomic positions were sequentially fully relaxed until convergence with the total energy tolerance on every atom of 10^{-4} eV.

Based on the first-principle calculations, the formation energies ΔH_f of the $L1_2$-$Co_{75}Al_{25-x}Nb_x$ can be calculated by the equation:

$$\Delta H_f = E - \frac{75}{100} E_{Co} - \frac{25-x}{100} E_{Al} - \frac{x}{100} E_{Nb} \quad (1)$$

where E is the internal energy per atom for the $L1_2$-$Co_{75}Al_{25-x}Nb_x$ alloy, E_{Co}, E_{Al}, and E_{Nb} are the internal energies per atom for pure hexagonal close-packed (HCP) Co, face-centered cubic

(FCC) Al, and body-centered cubic (BCC) Nb determined from the first-principle calculations, respectively.

The planar fault energies were calculated by employing the exact muffin-tin orbitals (EMTO) method [25, 26] to solve the Kohn-Sham equations. Electronic exchange and correlation were described by the generalized gradient approximation of Perdew-Burke-Ernzerhof functional [23]. The coherent potential approximation (CPA) [27, 28] is used to address the configurational disorder. The soft-core scheme and the scalar relativistic approximation were adopted. The *s*, *p*, *d*, and *f* orbitals were included in the muffin-tin basis set. The Brillouin zones for the $L1_2$ structure were sampled by 12 × 12 × 12 k-point meshes. The magnetic state of the phase at room temperature is determined before computing the planar fault energies. The Curie temperature (T_C) was evaluated using the mean-field approximation [29]:

$$T_C = \frac{2}{3k_B(1-c)}(E_{PM} - E_{FM}) \quad (2)$$

where k_B is the Boltzmann constant, c is the concentration of the nonmagnetic elements in the system, E_{PM} and E_{FM} are the total energies of phases in paramagnetic (PM) and ferromagnetic (FM) states, respectively. The paramagnetic state (PM) was simulated by the disordered local moments (DLM) model [30]. This model treats spin-up and spin-down components for each magnetic element as randomly distributed.

Thermodynamic calculations were performed by Thermo-Calc software via a Ni-based database (TTNI8). Two intermetallic phases (η and δ) were excluded during the thermodynamic evaluation since the TTNI8 database generally overestimates the stability of these two phases.

3. Results

3.1. Phase stability of the ordered $L1_2$-Co_3(Al, Nb) phase

The microstructure of the ternary Co-10Al-3Nb alloy (in at.%, this unit is applicable for the following content unless specified) after aging at 700 °C for 168 h is shown in **Fig. 1**. Low-magnification back-scattered electron (BSE) micrograph revealed an equiaxed grain structure with an average grain size of 36 ± 9 μm (**Fig. 1(a)**). Uniformly distributed high-density $L1_2$ precipitates throughout the γ-Co matrix were captured in **Fig. 1(b)**. In addition to the $L1_2$ precipitates, bulky B2-type CoAl phase was also observed mainly along grain boundaries, although a small amount of B2 phase was also located at grain interiors (**Fig. 1(b)**). The ordered nature of the $L1_2$ structure can be verified by the illuminated $L1_2$ precipitates in the dark-field TEM image (**Fig. 1(c)**), which is taken from the superlattice spot (**Fig. 1(d)**). The $L1_2$ phase appeared to percolate and aggregate along the ⟨100⟩ directions between neighboring particles. The diffraction pattern acquired from the B2 structure has also been shown in **Fig. 1(d)**.

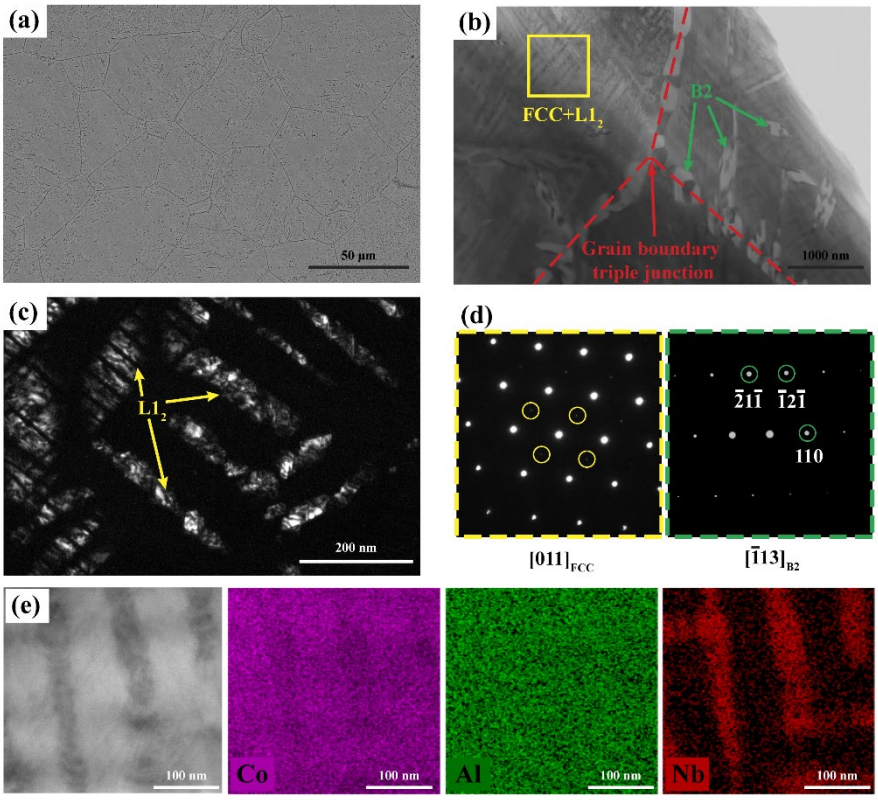

Fig. 1. (a) Back-scattered electron micrograph of the Co-10Al-3Nb alloy after aging at 700 °C for 168 h. (b) TEM micrograph of the magnified grain boundary triple junction region. Representative "FCC+$L1_2$" dual-phase region was highlighted in yellow. As pointed out by green arrows, the B2-type CoAl phase can be found both along grain boundaries and the grain interiors. (c) Dark-field TEM image showing well-aligned $L1_2$ particles. (d) Diffraction patterns took long [011] zone axis of the matrix phase and [$\bar{1}$13] zone axis of the B2-type CoAl phase. The $L1_2$ superlattice spots were highlighted in yellow circles. (e) EDS mapping of the "FCC+ $L1_2$" dual-phase region, showing Nb is strongly partitioned to the $L1_2$ particles.

Energy dispersive spectroscopy (EDS) mapping indicates that Nb is partitioned to the γ′ phase to a significant extent, whereas that of Al is marginal (**Fig. 1(e)**). The compositions of the matrix and the $L1_2$ phases were determined as Co-9.4±0.5Al-0.6±0.1Nb and Co-10.4±0.6Al-8.2±0.3Nb (at.%), respectively. According to the elemental partitioning study conducted by Omori et al. [7], elements partitioned to the γ′ precipitates are the γ′-stabilizing elements, otherwise the γ′-destabilizing elements. Therefore, both Al and Nb additions in the ternary Co-Al-Nb alloy contributed to the stability of the γ′ phase, which is in good agreement with previous DFT calculations [14, 17]. The total amount of the Al and Nb concentrations added up to 18.6 at.%, which is close to the expected stoichiometric amount among $L1_2$ structures. Therefore, the observed $L1_2$ precipitates can be referred to as the γ′-Co_3(Al, Nb) phase. The slight stoichiometric deviation should be ascribed to antisite occupation, the origin of which will be covered in the discussion part on the phase stability. Besides, the composition of the B2 phase was determined as Co-44.5±1.6Al-1.5±0.2Nb (at.%), suggesting a low solubility for the Nb in the B2 phase.

Previous studies indicated that the $L1_2$ phase was usually metastable among Co-based alloys and was prone to transform into equilibrium intermetallic phases [4, 18]. For example, it is reported that the ordered Co_3(Al, W) phase decomposed into the B2-type CoAl and $D0_{19}$-type Co_3W phases upon long-term aging treatments at 900 °C [2, 3]. Similarly, the γ-γ′ dual-

phase region was gradually replaced with the C36-type Laves phase and γ-Co matrix phase at 900 °C, suggesting the Laves phase was the equilibrium phase instead of the observed γ′ phase at an early stage of the heat treatment in the Co-6Ta-6V alloy [19]. Assuming it has already reached equilibrium after aging at 700 °C for 168 h, the remained γ′ phase suggested that the ordered $L1_2$ phase is thermodynamically stable at this temperature for the ternary Co-10Al-3Nb alloy. It is important to note that no stable $L1_2$ phase has been reported in the binary subsets (Co-Al, Co-Nb, and Al-Nb). Therefore, the formation of the stable γ′-Co_3(Al, Nb) phase in the ternary Co-Al-Nb alloy can be attributed to the stabilizing effect of Nb on the metastable γ′-Co_3Al phase. The role of alloying addition of Nb on stabilizing the $L1_2$ structure will be covered in the discussion part by first-principle calculations.

Figure 2(a) shows the XRD pattern of the Co-10Al-3Nb alloy after aging at 700 °C. Peaks belonging to the γ-γ′ two phases and B2-type CoAl intermetallic phase were clearly identified, which agree well with our microscopy observations. The asymmetric (002) peaks indicated a low degree of coherency between the γ and γ′ phases (see **Fig. 2(b)**), which were used for the peak deconvolution [31]. The lattice parameters were determined as 0.3644 nm and 0.3585 nm for the γ′ and γ phases, respectively. Lattice misfit was calculated to illustrate the constrained mismatch between the γ′ and γ phases, which can be derived as:

$$\delta = 2(a_{\gamma'} - a_{\gamma})/(a_{\gamma'} + a_{\gamma}) \quad (3)$$

where $a_{\gamma'}$ and a_{γ} are the lattice parameters for the γ′ and γ phases, respectively. Due to the larger lattice parameter of the γ′ phase compared to that of the γ phase, a positive constrained lattice misfit (+1.64 %) was maintained in the Co-10Al-3Nb alloy. It should be noted that such lattice misfit magnitude would probably be considered too large in the case of Ni-based superalloys. Large lattice misfits have also been previously reported among Co-Ti binary alloys with values of 0.75 - 1.67% [32]. Such high misfit caused the γ′-Co_3Ti phase to precipitate discontinuously in a cellular manner, which is unfavorable for mechanical properties [32, 33].

Instead of maintaining a spherical or cuboidal morphology, the γ′-Co_3(Al, Nb) precipitates appeared to grow directionally (**Fig. 1(c)**), which is a sign of the coherency loss at the γ/γ′ interface. Hence, balancing the lattice parameters of the γ′ and γ phases and effectively reducing the lattice misfit without coherency loss after long-term thermal exposure is vital for the development of the $L1_2$-strengthened Co-Al-Nb-based alloys for an advanced high-temperature performance.

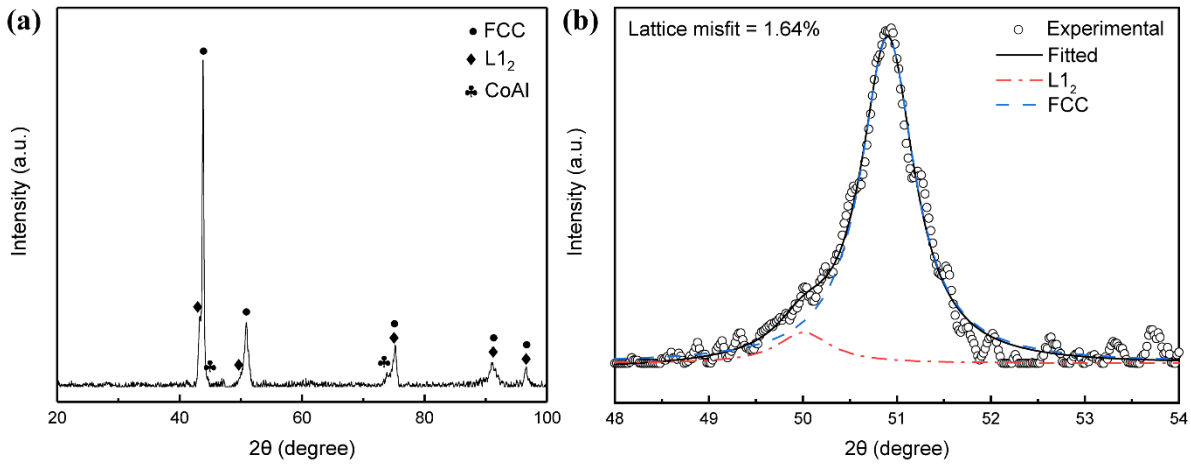

Fig. 2. (a) The X-ray diffraction patterns of the Co-10Al-3Nb alloy aged at 700 °C for 168 h. (b) Deconvolution of the asymmetric (002) peaks, showing peaks belonging to the FCC and $L1_2$ phases.

To probe the phase stability at elevated temperatures and the precipitation hardening effects, temporal microhardness evolution upon aging at 700 and 800 °C were shown in **Fig. 3(a)** for the current Co-10Al-3Nb alloy. The initial microhardness was 294 ± 10 HV after cooling from the recrystallization temperature. During isothermal aging at 700 °C, the microhardness value increased continuously with the prolonged aging time and reached 431 ± 15 HV after aging for 336 h. It is evident that the growth of precipitates, either or both of the $L1_2$ and B2 type precipitates strengthened the Co-10Al-3Nb alloy upon aging at 700 °C (**Fig.**

3(b)). In contrast with the continuously increased microhardness values at 700 °C, it dropped to ~250 HV when subjected to isothermal aging at 800 °C for merely 8 h. The γ′-Co_3(Al, Nb) precipitates vanished as the aging temperature increased to 800 °C and transformed into needle-shaped Laves phase (**Fig. 3(c)** and **Fig. S1**) [34]. The B2-CoAl phase can still be found at this temperature without dissolving into the γ-Co matrix. The decreased microhardness values imply a limited hardening effect for the remained B2-CoAl and Laves phases at 800 °C. Therefore, the significant strength increment at 700 °C should be mainly ascribed to the formation of high-density $L1_2$ precipitates.

The γ′-Co_3(Al, Nb) phase disappeared at 800 °C explains the reason for the lack of reports on the formation $L1_2$ phase among the ternary Co-Al-Nb alloys previously since the $L1_2$ structure is not thermodynamically stable once the aging temperature exceeds 800 °C, whereas the previous work only attempted to evaluate the equilibrium phase fields at higher temperatures in this alloy system [35, 36]. For example, Zhu et al. [36] use diffusion multiples to investigate the phase equilibria in the Co-rich part of the ternary Co-Al-Nb system at 900 °C. Clearly, these attempts fail to discover the $L1_2$ phase which only exists at a relatively lower temperature.

The absence of the $L1_2$ phase at 800 °C suggests the γ′-solvus temperature is lower than 800 °C in the present ternary Co-Al-Nb alloy. For comparison purposes, the γ′-solvus temperature is 990 °C for Co-9Al-9.8W alloy [1] and 964 °C for Co-5Al-14V alloy [37]. Since $L1_2$ precipitates provide a potent strengthening effect (**Fig. 3**), stabilizing the $L1_2$ phase towards higher temperatures is critical in the development of $L1_2$-strengthened Co-based high-temperature alloys. The approaches to stabilize the $L1_2$ phase in the baseline Co-Al-Nb alloy will be presented in the following section.

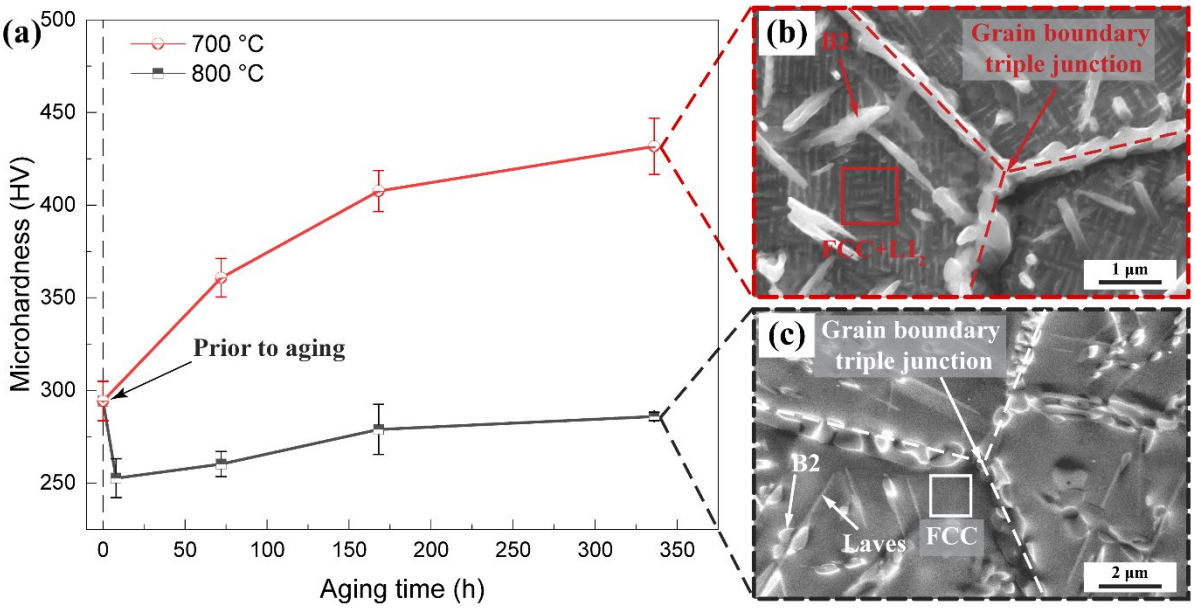

Fig. 3. (a) Temporal microhardness evolutions of the ternary Co-10Al-3Nb alloy aging at 700 °C and 800 °C, respectively. (b) SEM micrograph of the Co-10Al-3Nb alloy after aging at 700°C for 336 h, showing nanosized $L1_2$-type precipitates formation throughout the γ-Co matrix as well as blocky B2 phase. (c) SEM image of the Co-10Al-3Nb alloy after aging at 800 °C for 336 h. As the aging temperature increased to 800 °C, the γ′-Co_3(Al, Nb) phase disappeared and transformed into Laves phase.

3.2. Development of the $L1_2$-strengthened Co-Al-Nb-based alloys

Since advanced Ni-based superalloys rely on the γ′ precipitates to provide essential strength at elevated temperatures, effectively enhancing the stability of the γ′ phase and increasing the γ′-solvus temperatures are crucial in designing $L1_2$-strengthened alloys with enhanced temperature capabilities [5]. However, the γ′ precipitates were absent from the γ matrix at 800 °C in the ternary Co-10Al-3Nb alloy. Therefore, stabilizing the γ′ precipitates and elevating the γ′-solvus temperature via alloying additions are critically needed. It is reported that the Ni addition is capable of stabilizing the γ′ phase and broadening the γ-γ′ dual-phase region among Co-based alloys [7, 38]. For example, the Ni content is used to elevate the γ′-solvus temperature from 964 °C for the unmodified ternary alloy to 979, 1000, and 1032 °C

with the additions of 10, 20, and 30 at.% Ni in replacement of Co within the Co-Al-V-based alloys [37]. In addition to Ni content, Ti and Ta are also found to simultaneously stabilize the γ′ phase and enhance the mechanical properties within Co-based alloy systems [39, 40]. However, excessive Ti and Ta alloying additions may lead to detrimental TCP phase formation, such as $D0_{19}$ and μ phases [41, 42]. Therefore, it is worthwhile to explore the effects of these alloying additions with potential beneficial effects in the current Co-Al-Nb alloys. We attempt to stabilize the γ′ precipitates in the Co-Al-Nb-based alloys without inducing any brittle intermetallic phase formation via controlled alloying additions.

First, 15 and 30 at.% Ni additions were chosen to replace Co in the Co-10Al-3Nb alloy (referred to as base alloy). Therefore, Co-15Ni-10Al-3Nb and Co-30Ni-10Al-3Nb alloys were prepared, which are denoted as 15Ni and 30Ni alloys in the following content. The microstructures of the Ni-bearing alloys after aging at 700 °C for 168 h are shown in **Figs. 4(a-b)**. Apart from the γ′ precipitates and the γ matrix, we also identified a trace amount of the B2 phase at grain boundaries in the 15Ni alloy. More surprisingly, as the Ni addition further increased to 30 at.%, the B2 phase was eliminated completely, resulting in a clean γ-γ′ microstructure throughout the 30Ni alloy. **Figure 5(a)** shows the γ′-solvus and γ-solidus temperatures of the base, 15Ni, and 30Ni alloys. Ni addition increased the γ-solidus temperature from 1308 °C for the base alloy to 1341 °C for the 30Ni alloy. The relatively lower melting temperature among the base alloy is possibly associated with the Co-Nb eutectic reaction [43], which results in a notable decrease in the melting temperature. Therefore, Nb concentrations should be carefully controlled in designing $L1_2$-strengthened Co-based alloys with high melting temperatures. In addition to the increased γ-solidus temperature, Ni addition also substantially increased the γ′-solvus temperatures from 773 °C for the base alloy to 940 °C with 30 at.% Ni addition replacement. Given the beneficial alloying effects of the Ni additions in stabilizing the γ′ precipitates and suppressing brittle intermetallic phase formation, Co-Al-

Nb-Ni served as an alternative alloy system with a flexible compositional range and broader γ/γ′ phase region for developing $L1_2$-strengthened Co-Al-Nb-based high-temperature alloys.

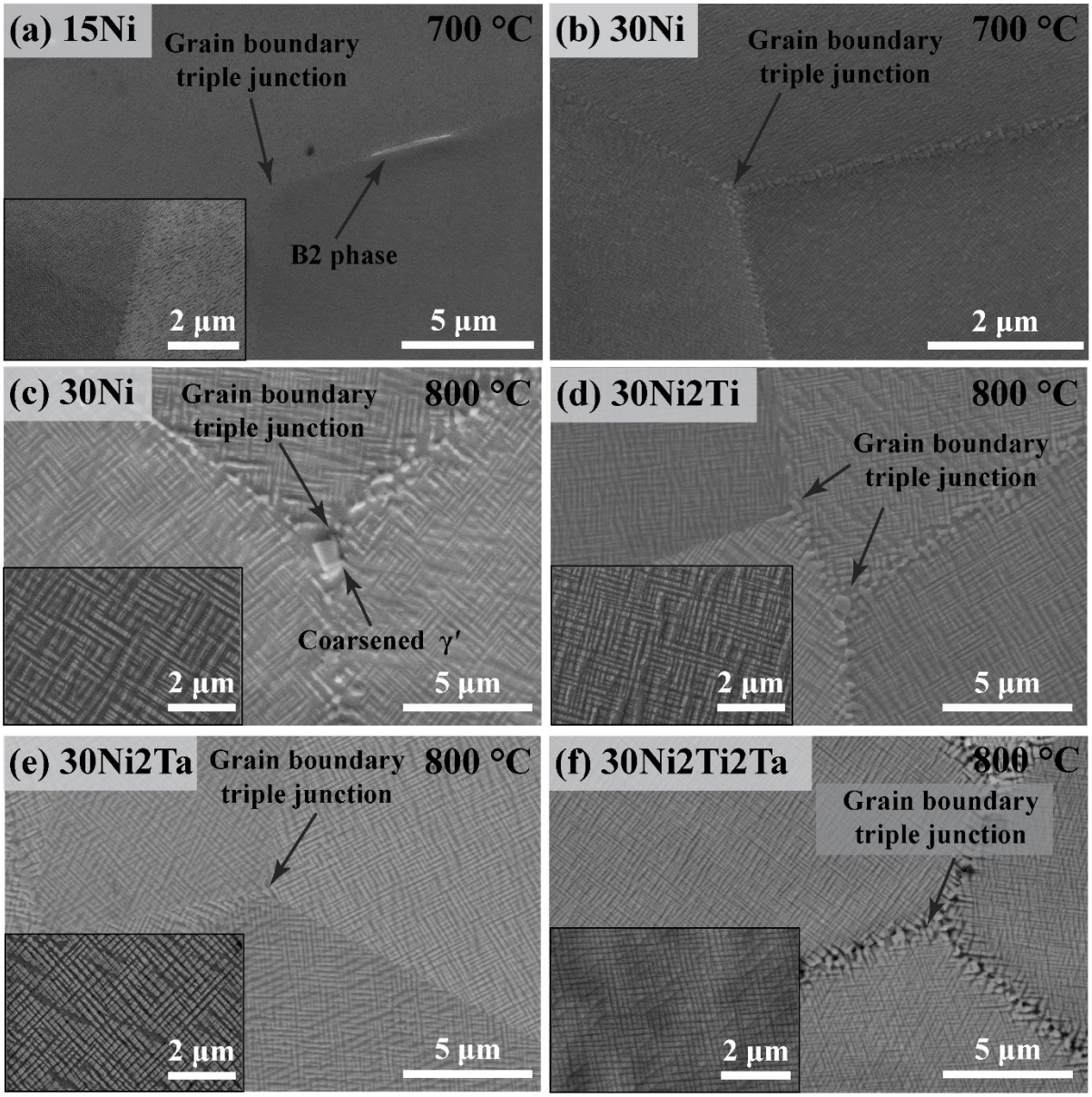

Fig. 4. Representative SEM micrographs of grain boundary triple junction region of the (a) Co-15Ni-10Al-3Nb (15Ni) and (b) Co-30Ni-10Al-3Nb (30Ni) alloys after aging at 700 °C for 168 h. A trace amount of the B2 phase was observed at grain boundaries for the 15Ni alloy, whereas a clean γ-γ′ dual-phase microstructure was maintained in the 30Ni alloy. Representative SEM micrographs of grain boundary triple junction region of the (c) Co-10Al-3Nb-30Ni (30Ni), (d) Co-10Al-3Nb-30Ni-2Ti (30Ni2Ti), (e) Co-10Al-3Nb-30Ni-2Ta (30Ni2Ta), and (f) Co-10Al-

3Nb-30Ni-2Ti-2Ta (30Ni2Ti2Ta) alloys after aging at 800 °C for 168 h. The enlarged grain interior micrographs are shown in the corresponding insets.

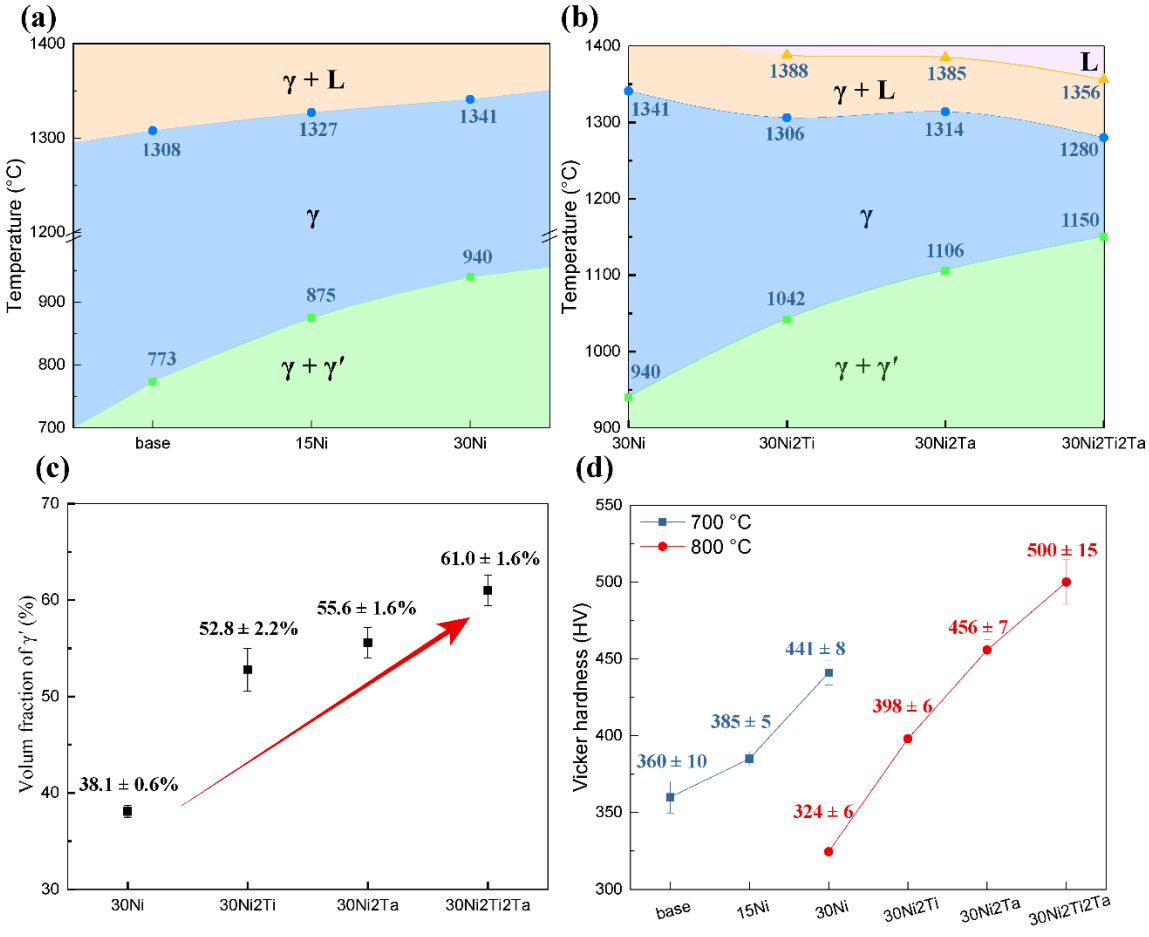

Fig. 5. (a) The γ′-solvus and γ-solidus temperatures of the base, 15Ni, and 30Ni alloys. (b) The γ′-solvus, γ-solidus, and liquidus temperatures of the 30Ni, 30Ni2Ti, 30Ni2Ta, and 30Ni2Ti2Ta alloys. (c) The volume fraction of the γ′ phase among the Co-Al-Nb-based alloys at 800 °C. (d) Microhardness evolutions of the Co-Al-Nb-based alloys after aging at 700 and 800 °C for 168 h.

Since the Co-30Ni-10Al-3Nb alloy exhibited a γ-γ′ dual-phase microstructure without other intermetallic phase formation, this alloy served as a baseline for further optimization. The Co-30Ni-10Al-3Nb-2Ti (30Ni2Ti) and Co-30Ni-10Al-3Nb-2Ta (30Ni2Ta) alloys were designed to investigate the alloying effect of Ti and Ta separately. Moreover, the combined

alloying effect of both Ti and Ta additions was also revealed in the Co-30Ni-10Al-3Nb-2Ti-2Ta (30Ni2Ti2Ta) alloy. Uniformly distributed γ′ precipitates embedded in the γ matrix was identified in the grain interior (see **Figs. 4(c-f)**), together with the coarsened γ′ precipitates at grain boundaries within the modified alloys after aging at 800 °C. A magnified view of the grain interior was shown in the corresponding inset. The alloying additions of Ti and Ta (2 at.%) did not induce other brittle intermetallic phase formation. In contrast, they were reported to induce W-rich $D0_{19}$ and μ phases formation at grain boundaries among Co-Al-W-based alloys [41]. Ti and Ta additions also substantially increased the γ′-solvus temperature: 2 at.% Ti and Ta alloying additions increased the γ′-solvus temperature to 1042 and 1106 °C, respectively (**Fig. 5(b)**). Moreover, the combined Ti and Ta alloying further stabilized the γ′-solvus temperature to 1150 °C, which is comparable with commercial Ni-based superalloys. Apart from the increased γ′-solvus temperature, the volume fraction of the γ′ phase (at 800 °C) also increased substantially by the alloying additions of Ti or Ta, from 38.1 ± 0.6% for the 30Ni alloy, to 52.8 ± 2.2% for the 30Ni2Ti alloy, and 55.6 ± 1.6% for the 30Ni2Ta alloy. The γ′ volume fraction further increased to 61.0 ± 1.6% for the 30Ni2Ti2Ta alloy (**Fig. 5(c)**). As a result of the increased volume fraction of the precipitates, the γ matrix channel became narrower via combined alloying additions of Ti and Ta compared with alloyed separately. These results confirmed the positive contribution from Ti and Ta alloying additions on the γ′ stability in the current Co-Al-Nb-based alloys.

Due to the enhanced γ′ phase stability and the elevated γ′ volume fraction in the Ni-bearing alloys, the microhardness values increased from 360 ± 10 HV for the base alloy to 385 ± 5 HV for the 15Ni alloy and 441 ± 8 HV for the 30Ni alloy after isothermal heat treatment at 700 °C for 168 h (**Fig. 5(d)**). Alloying additions Ti and Ta further strengthen the alloys: the microhardness increased progressively from 324 ± 10 HV for the 30Ni alloy, to 385 ± 5 HV for the 30Ni2Ti alloy, and 441 ± 8 HV for the 30Ni2Ta alloy after aging at 800 °C for 168 h

(**Fig. 5(d)**). The microhardness for the joint Ti and Ta alloying further increased to 500 ± 15 HV in the 30Ni2Ti2Ta alloy. The significantly improved microhardness can be partially attributed to the improved γ′ stability and the resultant elevated precipitation volume fraction in these modified alloys. More importantly, the incorporation of Ta and Ti substantially increased the planar fault energies [44], which increased the resistance from the γ′ precipitates to the shearing of the dislocations [45]. The stronger barriers to the dislocation shearing resulted in the overall strength improvement for the $L1_2$-strengthened Co-Al-Nb-based alloys.

Due to the sluggish diffusion kinetics and the resultant fine γ′ precipitation size, the specimens are annealed at 800 °C after cold-rolling to promote the solute diffusion and obtain a coarsened γ/γ′ microstructure [37, 46]. As shown in Fig. S2, the coarsened γ′ phase appeared bright in the back-scattered electron micrographs due to the refractory element enrichment. The compositions measured by SEM-EDS are shown in **Table 1**. Compositional analyses showed that the Co and Ni concentrations in the γ′ phase added up close to the stoichiometrically expected 75 at.% in the $L1_2$-type A_3B intermetallic compound. Therefore, it is expected that Al, Nb, Ta, and Ti atoms occupied the B sublattice site in the $L1_2$ phase [47, 48], i.e., the same sublattice site as occupied by the Al atoms in the $L1_2$-Ni_3Al phase. Therefore, the γ′ phase can be referred to as the γ′-$(Co, Ni)_3(Al, Nb, Ti, Ta)$ phase.

Table 1 The nominal and measured composition (in atomic percentage) of the Co-based alloys. The compositions of the γ and γ′ phases as determined from the coarsened phase regions are shown as well.

Alloy composition (at.%)		Elements					
		Co	Ni	Al	Nb	Ti	Ta
30Ni	Nominal	57.0	30.0	10.0	3.0	-	-
	Measured	56.8 ± 1.9	29.6 ± 0.9	10.5 ± 0.5	3.0 ± 0.8	-	-
	γ′-$L1_2$	42.5 ± 2.1	36.0 ± 0.9	14.8 ± 0.5	6.7 ± 0.8	-	-
	γ-FCC	67.7 ± 0.6	25.3 ± 0.2	6.1 ± 0.4	0.9 ± 0.1	-	-
30Ni2Ti	Nominal	55.0	30.0	10.0	3.0	2.0	-
	Measured	55.5 ± 1.5	28.9 ± 0.9	10.3 ± 0.3	3.1 ± 0.3	2.1 ± 0.2	-
	γ′-$L1_2$	42.5 ± 1.5	35.8 ± 0.9	13.2 ± 0.3	5.4 ± 0.3	3.1 ± 0.2	-
	γ-FCC	68.7 ± 0.2	21.9 ± 0.3	7.5 ± 0.3	1.0 ± 0.1	0.9 ± 0.1	-
30Ni2Ta	Nominal	55.0	30.0	10.0	3.0	-	2.0
	Measured	55.5 ± 1.8	29.0 ± 1.4	10.1 ± 0.2	3.2 ± 0.2	-	2.2 ± 0.2
	γ′-$L1_2$	42.0 ± 0.6	37.7 ± 0.7	11.4 ± 0.1	5.3 ± 0.2	-	3.6 ± 0.1
	γ-FCC	70.6 ± 0.6	23.1 ± 0.5	5.4 ± 0.1	0.6 ± 0.1	-	0.3 ± 0.1
30Ni2Ti2Ta	Nominal	53.0	30.0	10.0	3.0	2.0	2.0
	Measured	53.6 ± 1.8	29.2 ± 1.4	9.8 ± 0.2	3.2 ± 0.2	2.2 ± 0.1	2.0 ± 0.2
	γ′-$L1_2$	44.4 ± 1.8	35.5 ± 1.4	10.6 ± 0.2	4.0 ± 0.2	2.8 ± 0.1	2.7 ± 0.2
	γ-FCC	72.0 ± 0.5	20.5 ± 0.3	5.6 ± 0.1	0.9 ± 0.1	0.7 ± 0.1	0.3 ± 0.1

To quantitatively describe the elemental partitioning behavior in the Co-Al-Nb-based alloys, partitioning coefficients K are calculated and plotted in **Fig. 6**, which can be derived as [8]:

$$K_i = C_i^{\gamma'}/C_i^{\gamma} \quad (4)$$

where $C_i^{\gamma'}$ and C_i^{γ} are the atomic concentration of the element *i* in γ′ and γ, respectively. As we can see, only Co was partially depleted from the γ′ precipitates and partitioned to the γ matrix, whereas all the other elements were partitioned to the γ′ precipitates, including Al, Nb, Ni, Ti, and Ta. Specifically, Ni and Al were partially partitioned to the γ′ precipitates (K_{Ni} = 1.42 and K_{Al} = 2.43) in the 30Ni alloy. The alloying additions of Ti and Ta increased the propensity for Ni to partition to the γ′ precipitates, whereas suppressed the Al from entering the γ′ phase. Since

Al atoms shared the same sublattice site as Ti and Ta atoms [47, 48], the additions of Ti and Ta occupied part of the sublattice site in the A_3B-type $L1_2$ phase which could have been taken up by Al atoms. Therefore, the degree for Al to partition to the γ′ precipitates was weakened by Ti and Ta alloying additions. Besides, Nb, Ti, and Ta demonstrated a strong tendency to partition to the γ′ precipitates ($K_i > 4$). Such high partitioning coefficient values imply that Nb, Ti, and Ta have a profound influence on the γ′ phase formation and contribute to the stability of the γ′ phase [7]. Elemental partitioning behaviors are consistent with previous findings in the Co-Al-W-based alloy systems [41, 42, 49]. These findings agree well with the increased γ′-solvus temperatures and elevated γ′ volume fractions with Ti and Ta alloying (see **Fig. 5**). Therefore, Ti, Ta, and Nb are crucial for stabilizing the $L1_2$ precipitates in the multicomponent Co-rich alloys.

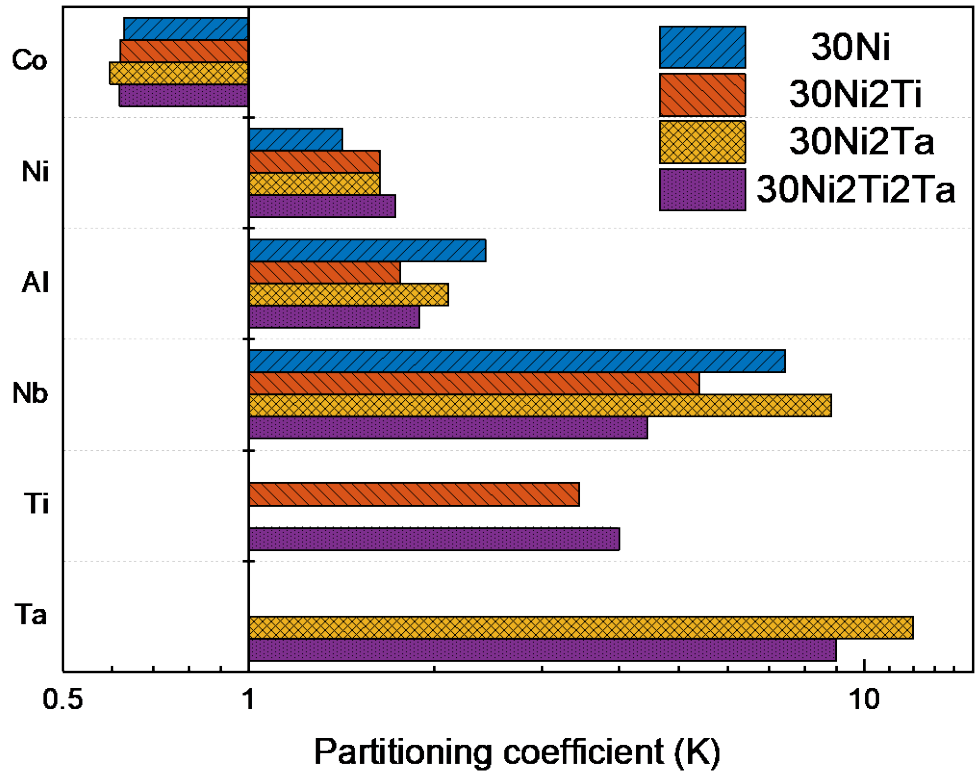

Fig. 6. Elemental partitioning coefficients K_i of the multicomponent Co-rich alloys, showing Co partitioned to the γ matrix phase, whereas Ni, Al, Nb, Ti, and Ta partitioned to the γ′ precipitates.

Given the enhanced γ′ stability (1150 °C for the γ′-solvus temperature) as well as the remarkable microhardness after the long-term thermal exposure (500 ± 15 HV after aging at 800 °C for 168 h), the 30Ni2Ti2Ta alloy served as a promising candidate among the $L1_2$-strengthened Co-Al-Nb-based alloy systems to probe the potential for high-temperature applications. The microstructure of the 30Ni2Ti2Ta alloy and corresponding schematic diagram are shown in **Figs. 7(a-b)**. High-density cuboidal γ′ precipitates were arranged regularly in the γ matrix phase. As illustrated in the reconstructed APT nanotip, a narrow γ channel was sandwiched between two adjacent γ′ particles with flat γ/γ′-heterophase-interfaces (**Fig. 7(c)**). Moreover, there is a distinguished composition difference between the γ and γ′ phases with Co partitioning essentially to the γ matrix, while the rest elements, namely Ni, Al, Nb, Ti, and Ta, partitioning to the γ′ phase. 1D concentration profiles for the constituent elements across the γ/γ′ interfaces were shown in **Fig. 7(d)**, which further confirms the strong partitioning behavior of Nb, Ti, and Ta to the γ′ phase with less than 1 at.% left in the γ matrix phase.

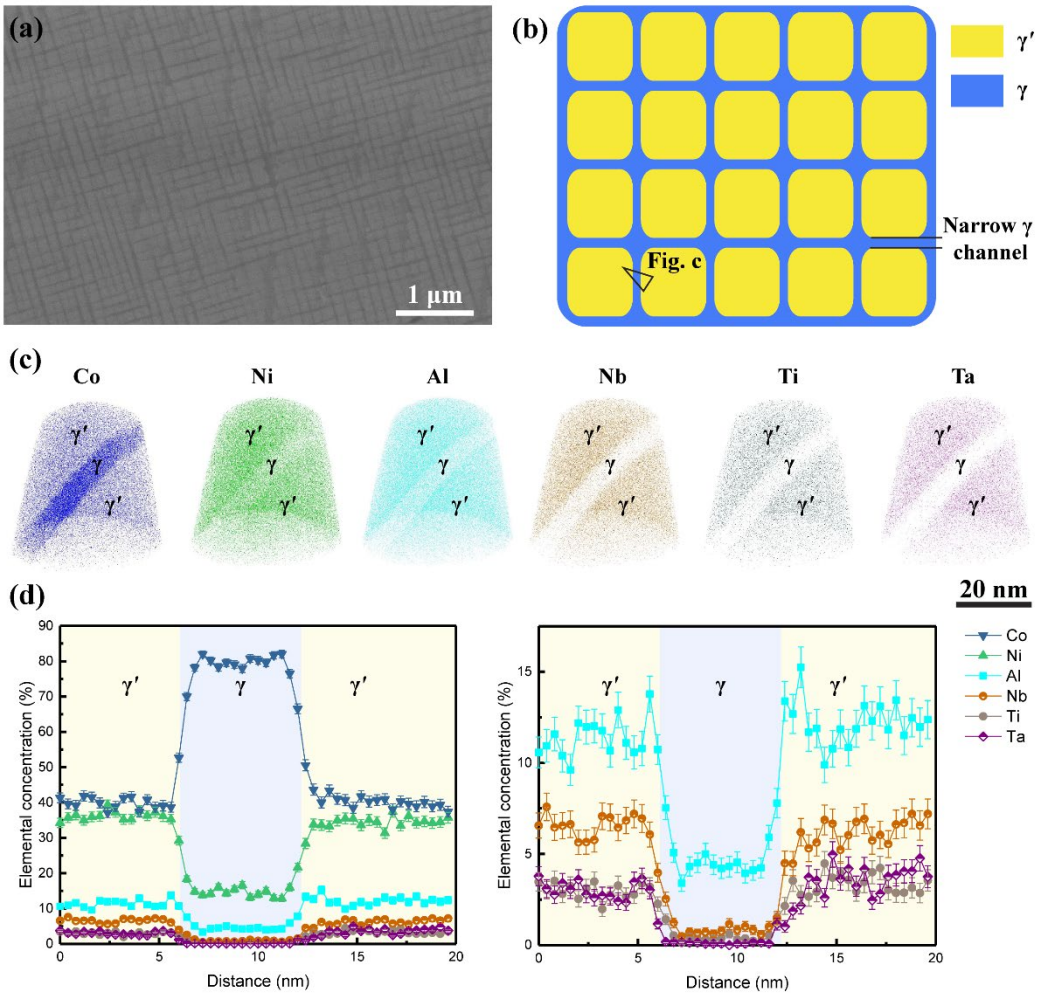

Fig. 7. (a) SEM micrograph of the 30Ni2Ti2Ta alloy and (b) corresponding schematic diagram, showing that high-density γ′ precipitates divide the γ phase into nanoscale channels. (c) Ion maps of reconstructed nanotips by APT. (d) Proximity histograms across the γ/γ′ interfaces, showing distinctly different elemental compositions between the γ and γ′ phases.

3.3. Mechanical properties and matrix-confined stacking-faults-mediated deformation

The 0.2% compressive yield strength of the 30Ni2Ti2Ta alloy has been shown in **Fig. 8** as a function of deformation temperatures. The yield strength reached the gigapascal level (1023 ± 27 MPa) at ambient temperature. It gradually decreased to 833 ± 21 MPa as the deformation temperature increased to 600 °C. Interestingly, the yield strength anomaly was observed in the temperature range between 600 and 700 °C with an increased yield strength to

897 ± 53 MPa at 700 °C. Above 700 °C, the yield strength started to decrease again and dropped to 459 ± 57 MPa at 900 °C. For comparison purposes, the strength of Haynes 188 [50] (a conventional carbide-strengthened Co-based alloy), Waspaloy [50] (a commercial Ni-based superalloy), Co-11Ti-15Cr, Co-9Al-9W, Co-30Ni-12Al-4Ta-12Cr, and Co-30Ni-10Al-5V-4Ta-2Ti alloys [37, 46, 51, 52] ($L1_2$-strengthened Co-based alloys) at various deformation temperatures were also included in **Fig. 8**. The strength of the 30Ni2Ti2Ta alloy exceeded that of Co-11Ti-15Cr and Co-9Al-9W Co-based alloys strengthened by the $L1_2$ precipitates, which can be primarily attributed to the enhanced particle stability at elevated temperatures and associated particle shearing resistance. The yield strength of 30Ni2Ti2Ta was even superior to Ni-based superalloy Waspaloy over the entire temperature range. To get insight into the detailed deformation behavior, the deformation substructures of the present 30Ni2Ti2Ta alloy at ambient and elevated temperatures have been carefully examined via transmission electron microscopy in the following content.

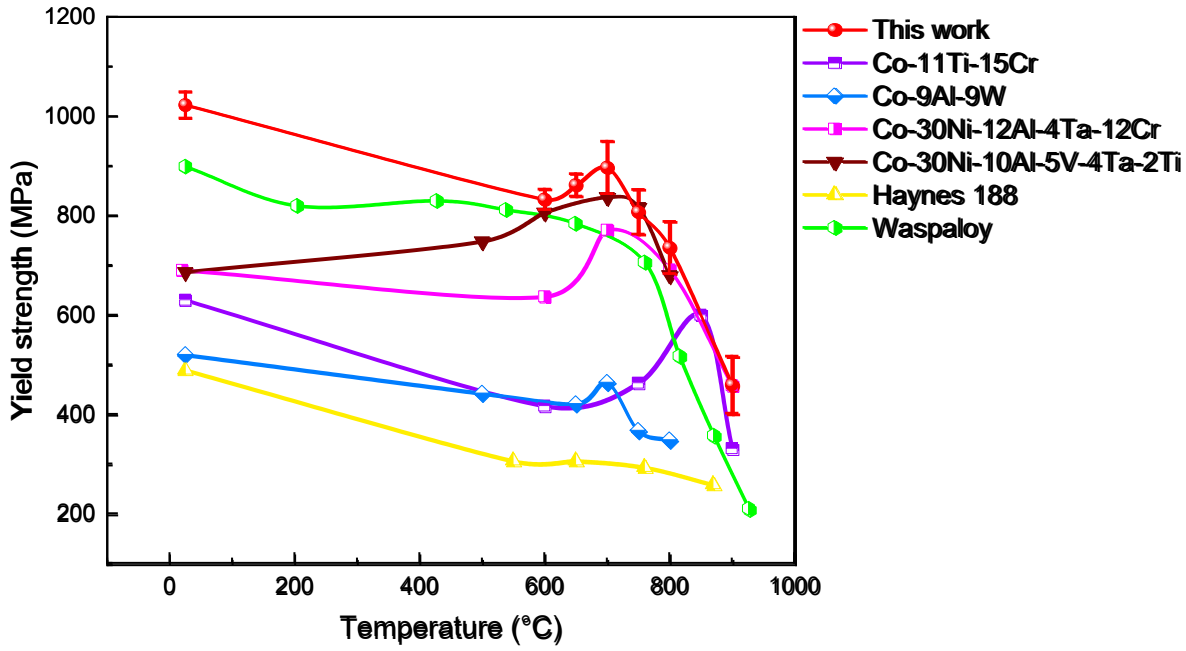

Fig. 8. The plots between the yield strength and deformation temperature of the 30Ni2Ti2Ta alloy, together with other $L1_2$-strengthened Co-based alloys (Co-11Ti-15Cr, Co-9Al-9W, Co-

30Ni-12Al-4Ta-12Cr, and Co-30Ni-10Al-5V-4Ta-2Ti alloys), a conventional carbide-hardened Co-based alloy (Haynes 188), and a commercial Ni-based superalloy (Waspaloy).

Figure 9 presents the typical structural features of the 30Ni2Ti2Ta alloy deformed at room temperature. Specimens were prepared by interrupted compression test after ~2% plastic deformation. TEM bright-field and dark-field micrographs witnessed the formation of high-density stacking faults within the matrix channels (**Fig. 9(a)**). Thus, the plastic deformation was concentrated in the γ channels and governed predominately by stacking faults. The structure of the stacking fault was further examined via high-resolution TEM. As shown in **Figs. 9(b-d)**, the extension of the stacking faults has been hindered by the γ′ precipitates and got stopped at the γ/γ′ interfaces without shearing through even with a plastic strain of ~2%. Various deformation substructures have been previously reported among the $L1_2$-strengthened superalloys. For example, the penetration of a/2<110> dislocation pairs into γ′ precipitates together with anti-phase boundary ribbon was identified as a result of γ′ cutting among Ni-based superalloys [53]. Extensive stacking faults, both superlattice intrinsic stacking faults (SISFs) and superlattice extrinsic stacking faults (SESFs), extending across the whole γ′ particles have been observed among Co-based superalloys after 2% creep deformation at 900 °C [54]. Shearing of the γ′ particles can also be accompanied by other complex fault configurations, such as SISF loops embedded within APBs as well as SISF ribbon coupled with two adjacent APBs [55]. However, none of these abovementioned shearing configurations are consistent with the deformation substructures as identified here, in which no detectable straining has been sustained by the γ′ precipitates under such circumstance. The stacking faults are geometrically confined in the narrow matrix channels without extending into neighboring γ′ particles.

The formation of the matrix-confined stacking faults has also been frequently observed among the specimens subjected to deformation at 700 °C with a plastic strain of ~2% (**Fig.**

10(a)). Apart from that, the shearing of the particles by superlattice stacking faults (SSFs) has been observed within the 30Ni2Ti2Ta alloy after the interrupted compression test at this temperature (**Fig. 10(b)**). The interactions of such planar faults have been speculated to be the origin for the yield anomaly at this temperature, which will be introduced in the discussion part. **Figure 11** shows the schematic diagrams of the deformation substructures of the 30Ni2Ti2Ta alloy after ~2% plastic deformation both at 25 and 700 °C.

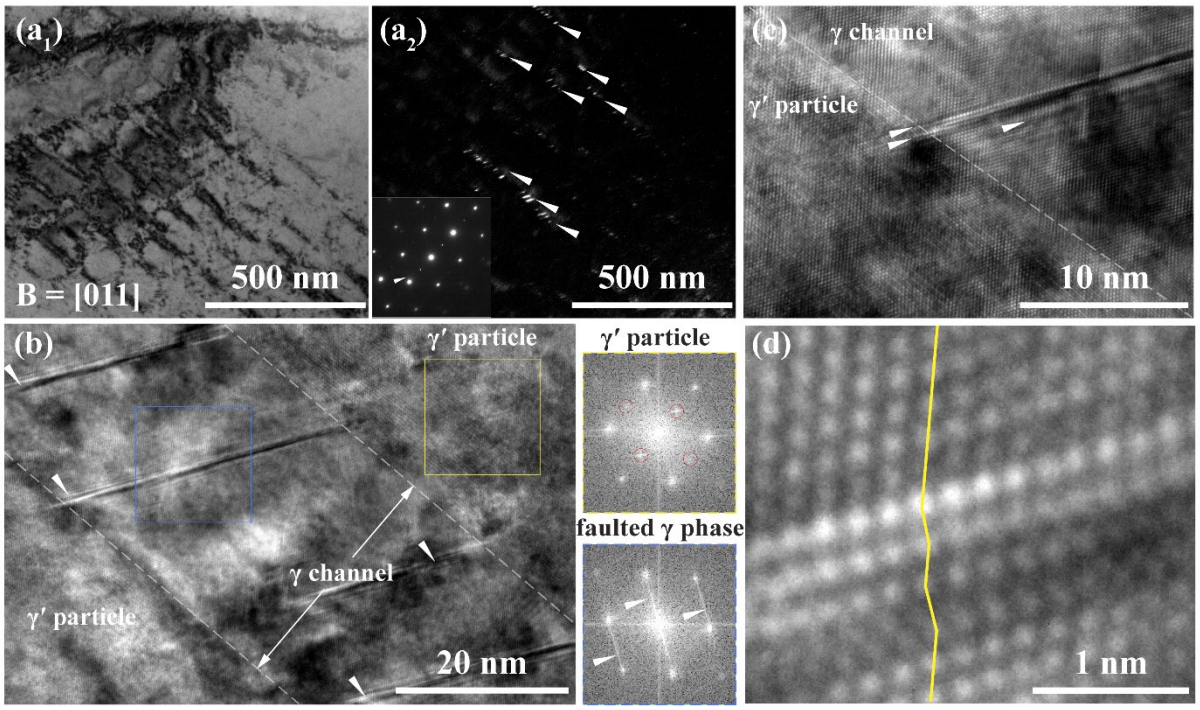

Fig. 9. (a) TEM bright-field (BF) and dark-field (DF) micrographs of the 30Ni2Ti2Ta alloy after ~2% plastic deformation at room temperature. High-density γ′ precipitates were found to be separated by narrow matrix channels. The weak streaking lines (as highlighted by white arrow) in the corresponding diffraction pattern (inset) indicated the presence of stacking faults. DF micrograph was taken using the streaking lines, which illuminated numerous matrix-channel-confined stacking faults. (b) High-resolution TEM (HRTEM) image gave a closer view of the matrix-confined stacking faults. The Fast Fourier Transform (FFT) diffraction patterns taken from the γ′ particles (yellow square) and the γ matrix channels containing stacking faults (blue square) have been shown as well. Superlattice spots have been highlighted by red circles, indicating the ordered nature of the γ′ particles. Streaking lines can be found in the FFT of the faulted γ matrix phase (as pointed out by white arrows), which also confirmed the existence of stacking faults among matrix channels. (c) Representative HRTEM image

demonstrated the extension of the stacking faults via partial dislocations was hindered by the γ′ precipitates and stopped at the γ/γ′ interfaces. (d) HRTEM micrograph showing the atomic structure of the stacking fault region.

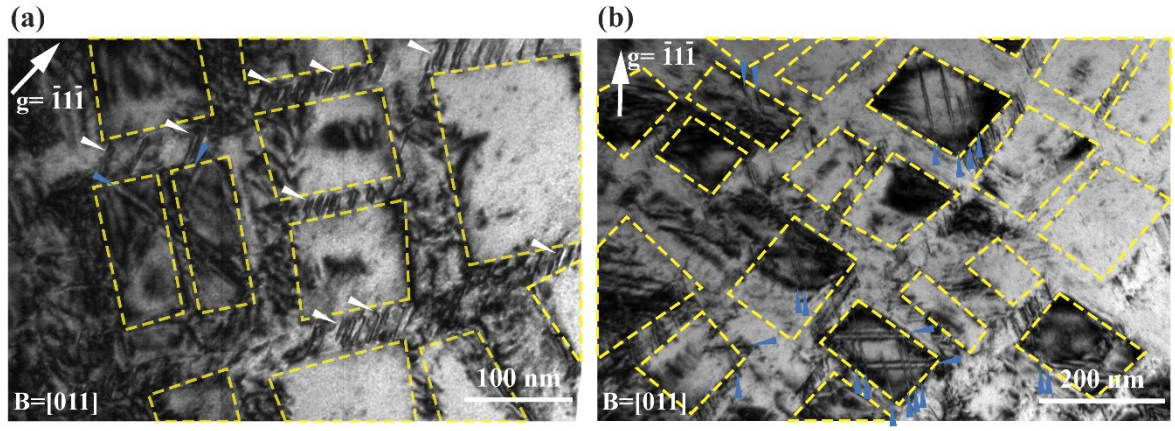

Fig. 10. TEM micrographs of the 30Ni2Ti2Ta alloy deformed at 700 °C with a plastic strain of ~ 2%. Cuboidal γ′ precipitates (yellow squares) distributed uniformly across the matrix phase. High-density stacking faults were observed in the matrix channel, as indicated by white arrows. Particle shearing via superlattice stacking faults (SSFs) was activated at this temperature (blue arrow).

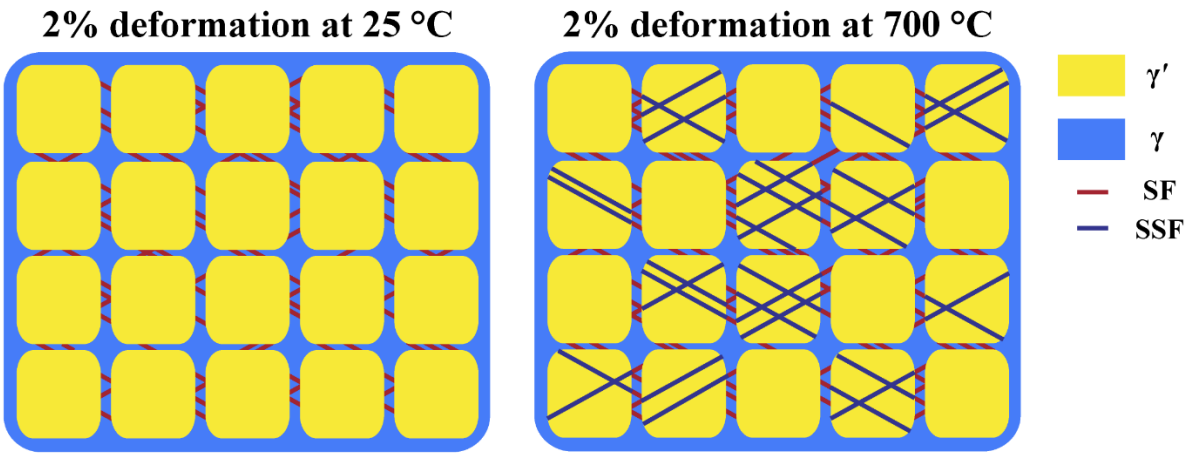

Fig. 11. Schematic diagrams of the deformed substructures at 25 and 700 °C. Abbreviations: SF, stacking fault; SSF, superlattice stacking fault.

4. Discussion

4.1. Phase stability of the $L1_2$-type Co_3(Al, Nb) intermetallic phase

The experimentally observed $L1_2$-Co_3(Al, Nb) precipitates are in line with the recent theoretical first-principle calculations which indicated that the $L1_2$-type $Co_3(Al_{0.5}, Nb_{0.5})$ phase exhibited the lowest formation energy among several transition-metal-stabilized $L1_2$-type $Co_3(Al_{0.5}, TM_{0.5})$ (TM = Nb, Cr, Re, V, Ti, Ta, W, Mo) intermetallic phases at 0 K [16]. In other words, Nb is the most favorable element in enhancing the stability of the $L1_2$ structure. Moreover, the $L1_2$ phase can be further stabilized by the entropy contribution at finite temperatures when taking entropy contributions (e.g., lattice vibration, thermal electronic excitation, and mixing configuration) into consideration [16]. Given the fact that the composition of the current Co_3(Al, Nb) strengthener differs from the stoichiometric ratio as used in the recent first principle study, we further investigate the effect of elemental concentrations on the phase stability of the newly-found $L1_2$-Co_3(Al, Nb) phase.

To evaluate the chemical stability of the $L1_2$-type intermetallic phase, the enthalpy formation energy ΔH_f of the $L1_2$-$Co_{75}Al_{25-x}Nb_x$ phase is plotted as a function of the Nb concentration in **Fig. 12**. Our calculated ΔH_f of the $L1_2$-type Co_3Al phase was -0.1622 eV/atom (see **Table 2**). As shown in **Fig. 12**, the adding of the minor Nb content into the $L1_2$-type Co_3Al phase shifted the ΔH_f into more negative values. The ΔH_f reached the minimum for the $L1_2$-Co_3(Al, Nb) phase containing 10 at.% Nb (-0.1703 eV/atom). Beyond this point, the ΔH_f started to increase as the Nb concentration increased. Therefore, minor Nb alloying (~ 10 at.%) is favorable in stabilizing the $L1_2$ structure among CoAl-based alloys. In fact, as examined by TEM-EDS, the Nb concentration in the $L1_2$-type Co_3(Al, Nb) precipitates was 8.2 ± 0.3 at.%, which is close to the most stable composition as predicted via the *ab initio* approach. It should be noted that we only consider the effect of Nb concentration on the phase stability of the $L1_2$ structure here, and the effect of antisite occupation has not been covered since we deliberately fix the stoichiometric ratio to 3:1 for the $L1_2$ intermetallic phase. In fact, the total atomic compositions of Al and Nb added up to ~18.6 at.% in the γ′ phase, which are somewhat lower

than the expected 25 at.% for the "ideal" A_3B-type $L1_2$ phase. As a compensation for the shortage of Al and Nb contents, excess Co addition partially occupied the Al and Nb sublattice site to balance the stoichiometric ratio. Previous investigations towards Co-based $L1_2$ phases also reported excess Co concentrations, such as the γ′-Co_3(Al, V), γ′-Co_3(Al, Mo, Ta), γ′-Co_3(Al, W), and γ′-Co_3Ti [37, 56-58]. The excess Co content is believed to shift the Fermi level towards the pseudogap, leading to an increased total number of *d*-electrons. The resultant more bonding states contribute to the improved structural stability of the $L1_2$ phase [57]. The effect of antisite occupation among Co_3(Al, Nb) on the phase stability of the $L1_2$ structure needs further exploration.

Table 2 Enthalpy formation energies of the $L1_2$-type Co_3(Al, Nb) phase with varied Nb concentrations.

	ΔH_f (eV/atom)
$Co_{75}Al_{25}$	-0.1622
$Co_{75}Al_{22}Nb_3$	-0.1629
$Co_{75}Al_{19}Nb_6$	-0.1697
$Co_{75}Al_{15}Nb_{10}$	-0.1703
$Co_{75}Al_{10}Nb_{15}$	-0.1626
$Co_{75}Al_5Nb_{20}$	-0.1531
$Co_{75}Nb_{25}$	-0.1460

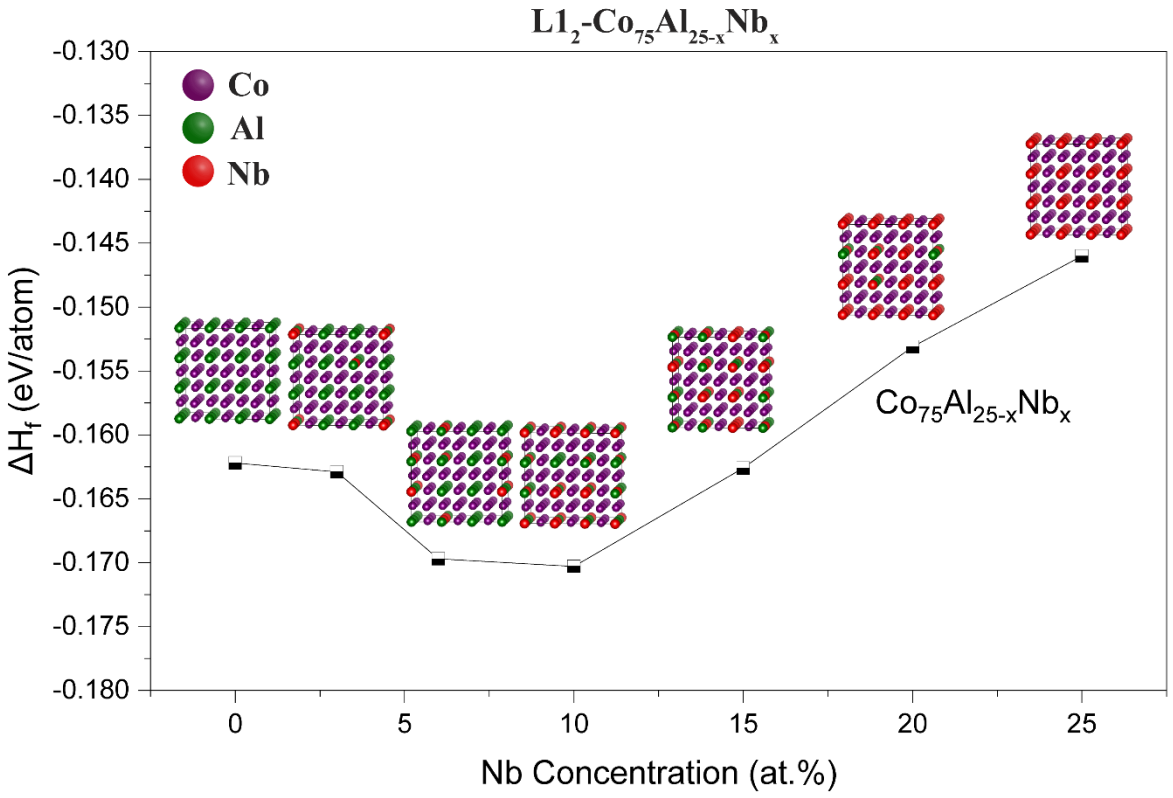

Fig. 12. Enthalpy formation energies of the $L1_2$-type Co_3(Al, Nb) phase as a function of Nb concentrations (0, 3, 6, 10, 15, 20, 25 at.%).

4.2. Effect of alloying additions on the microstructural evolutions of the Co-Al-Nb-based alloys

The dispersed B2 phase was identified in the ternary Co-Al-Nb phase after aging at 700 °C. However, by comparing the microhardness values upon isothermal aging at 700 and 800 °C (**Fig. 3**), it is believed that the dispersed B2 phase contributed little to the strength of the alloys. Additionally, the formation of the B2 phase also depleted the Al content from the matrix phase, which could have been used to induce the $L1_2$ phase formation and increase the volume fraction of the $L1_2$ strengtheners. More importantly, the incoherent interfaces between the B2 and the γ-Co phase are likely to cause severe stress localizations, leading to a brittle fracture during the tensile deformation. Luckily, the alloying addition of the Ni content was

found to suppress the B2 phase formation: 15 at.% Ni avoided the formation of the intragranular B2 phase, leaving a trace B2 phase occasionally located at grain boundaries; 30 at.% Ni completely refrained the B2 phase from its formation, resulting in a clean γ-γ′ dual-phase microstructure. To rationalize the reason for the suppression of the B2 phase formation with alloying additions of Ni, thermodynamic calculations were performed to provide a fundamental understanding towards such microstructural transitions.

As illustrated in **Fig. 13(a)**, the fraction of the B2 and $L1_2$ phases are plotted at a function of the Ni concentration among the Co-10Al-3Nb-*x*Ni alloys. Thermodynamic calculations revealed that the phase fraction of the B2 phase started to increase marginally with the Ni content at low concentration ($<$ 7.5 at.%); however, the B2 phase is destabilized at a higher Ni concentration and quickly vanished at the ~17.5 at.% Ni concentration. These results agree well with our experimental observations that only a trace amount of the B2 phase can be found in the 15Ni-alloyed specimen. Our thermodynamic calculations predict that the $L1_2$ phase does not exist in the Ni-free alloy, which seems to deviate from our experimental results at first glance. However, it is important to note that the phase equilibria of the $L1_2$-Co_3(Al, Nb) phase have not been evaluated in the thermodynamic database, and therefore it is not difficult to understand the reason for the failure to predict the $L1_2$ phase formation in the ternary Co-Al-Nb alloy. Thermodynamic calculations suggest that the emergence of the $L1_2$ structure started at ~ 8.3 at.% Ni and its phase fraction increased rapidly to around 50% with 30 at.% Ni. These predictions suggest that the alloying addition of Ni can not only suppress the B2 phase formation, but also can increase the volume fraction of the $L1_2$ phase, which is in line with the observed microstructural evolution trend.

Apart from Ni, another two beneficial elements have also been identified in the current study for the improved $L1_2$ stability, that is, Ti and Ta. Our experimental results suggest that alloying additions of Ti and Ta (2 at.%) helps to enhance the stability of the $L1_2$ structure. The

$L1_2$ precipitates can be further stabilized via combined Ti and Ta alloying with the increased γ′-solvus temperature to 1150 °C for the 30Ni2Ti2Ta alloy, which is vital for the potential application of $L1_2$-strengthened Co-rich alloys towards elevated temperature environments. As presented in **Fig. 13(b)**, we calculated the phase fraction of the $L1_2$ structure as a function of aging temperature among the Co-Al-Nb-based alloys, which showed the positive contributions from both Ti and Ta to the $L1_2$ phase fraction and the γ′-solvus temperature. These predictions are consistent with our experimental observations that the Ti and Ta alloying additions are favorable for the $L1_2$ stability.

It should be noted that the oxidation resistance should be taken into considerations in the current Co-Al-Nb-based alloys since a sufficient oxidation resistance is a prerequisite for high-temperature structural materials. Continuous Al_2O_3 and Cr_2O_3 scales are favorable in providing potent oxidation resistances, and the formation of such scales are feasible through balanced alloying additions, e.g., Al, Cr, and Si contents [59, 60]. Therefore, more efforts are still needed to enhance the oxidation resistance of the Co-Al-Nb-based alloys through carefully studying their alloying effects.

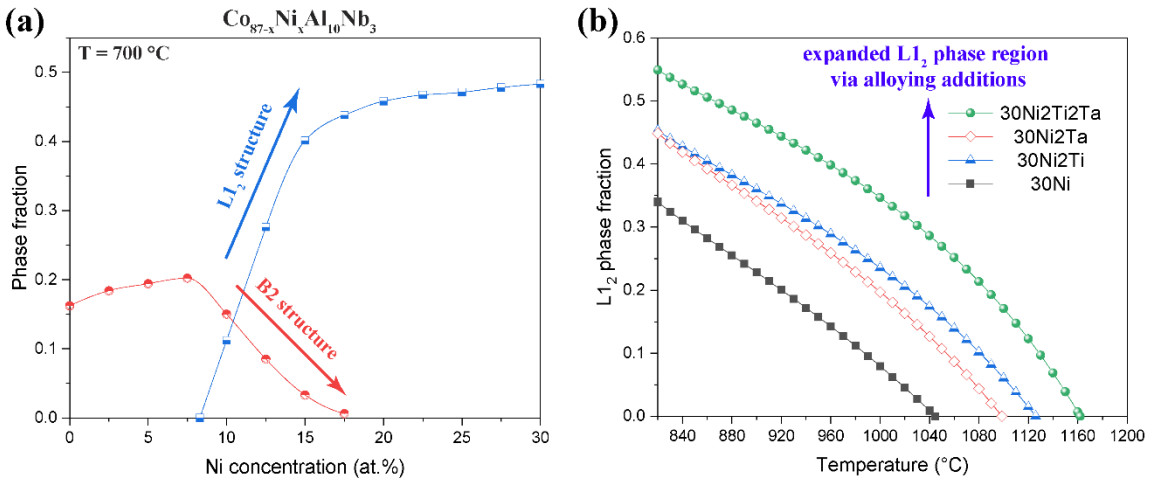

Fig. 13. (a) Phase fraction of the $L1_2$ structure and the B2 structure as a function of Ni concentration in the Co-10Al-3Nb-*x*Ni alloy. (b) $L1_2$ phase fraction as a function of temperature among Ti- and Ta-alloyed Co-10Al-3Nb-30Ni-based alloys.

4.3. Matrix-confined stacking faults formation

Our previous TEM observations indicated that the matrix-confined stacking faults acted as the primary plasticity carriers in the present alloy. The low stacking fault energy matrix together with the narrow matrix channel is expected to promote the dissociation of the a/2<110> perfect dislocation into two a/6<211>-type Shockley partials and the associated stacking fault formation in between the partials [61].

According to the Orowan model, the critical resolved shear stress τ_D, required for perfect dislocations gliding within a confined volume (restricted in the narrow matrix channel), can be written as [62]:

$$\tau_D = \frac{Gb}{D} \quad (5)$$

where G is the shear modulus of the γ matrix, b is the Burgers vector of a perfect dislocation, and D is the mean free path of dislocations in the matrix channels along <110> directions. Due to the concentrated cobalt content in the matrix phase (~ 80 at.%), the shear modulus of the matrix phase G is estimated from a FCC-structured Co-based alloy using experimentally determined elastic constants as follows: C_{11} = 184.4 GPa, C_{12} = 99.8 GPa, C_{44} = 137.4 GPa [63]. Voigt et al. [64] and Reuss et al. [65] have determined both the upper bound and the low bound of the shear modulus, respectively. Herein, we apply Hill's approach to calculate shear modulus by averaging Reuss and Voigt's approaches [66]. Therefore, G is determined as 85.9 GPa. Burgers vector of a perfect dislocation b is a/2 <110>, where a is the lattice parameter of the matrix phase. The lattice parameter of the matrix phase was obtained by deconvolution of the XRD peaks from the (311) plane, which was determined as 0.3598 nm (see **Fig. S3**). In this way, b is calculated as 0.2544 nm. Mean dislocation free path D was determined as 27 nm based on the HRTEM images taken along the [011] zone axis (see **Fig. 9(b)**). Therefore, the critical resolved shear stress for perfect dislocation gliding in the matrix channel is estimated to be ~809 MPa. Assuming an average Schmid factor of 0.326 for polycrystalline FCC-

structured materials [67], the corresponding critical uniaxial applied stress is estimated to be ~2482 MPa, which is far above the tensile stress after plastic strained for ~2%. Next, we calculated the critical resolved shear stress required for the perfect dislocation dissociation and associated stacking faults formation.

Most of the stacking faults have been found to extend across the entire matrix channels and terminated at the γ/γ′ interfaces. Herein, we assume that the observed stacking faults could extend continuously, if they were not hindered by the γ′ precipitates (the origin of γ′ phase on blocking the extension of stacking faults will be discussed in the next section). It is proposed that the critical resolved shear stress, τ_{SF}, required for spontaneous partial dislocation separation and associated extended stacking fault formation is given as [68]:

$$\tau_{SF} = \frac{2\gamma_{SF}}{b_P} \quad (6)$$

where γ_{SF} is the stacking fault energy of the γ matrix, and b_P is the Burgers vector of a Shockley partial dislocation. According to the lattice parameter determined by the XRD peak deconvolution (see **Fig. S3**), Shockley partial dislocation b_P is determined as 0.1469 nm. It should be noted that the value derived here is an upper bound of the critical resolved shear stress required for dislocation dissociation since we assume an infinite stacking fault extension.

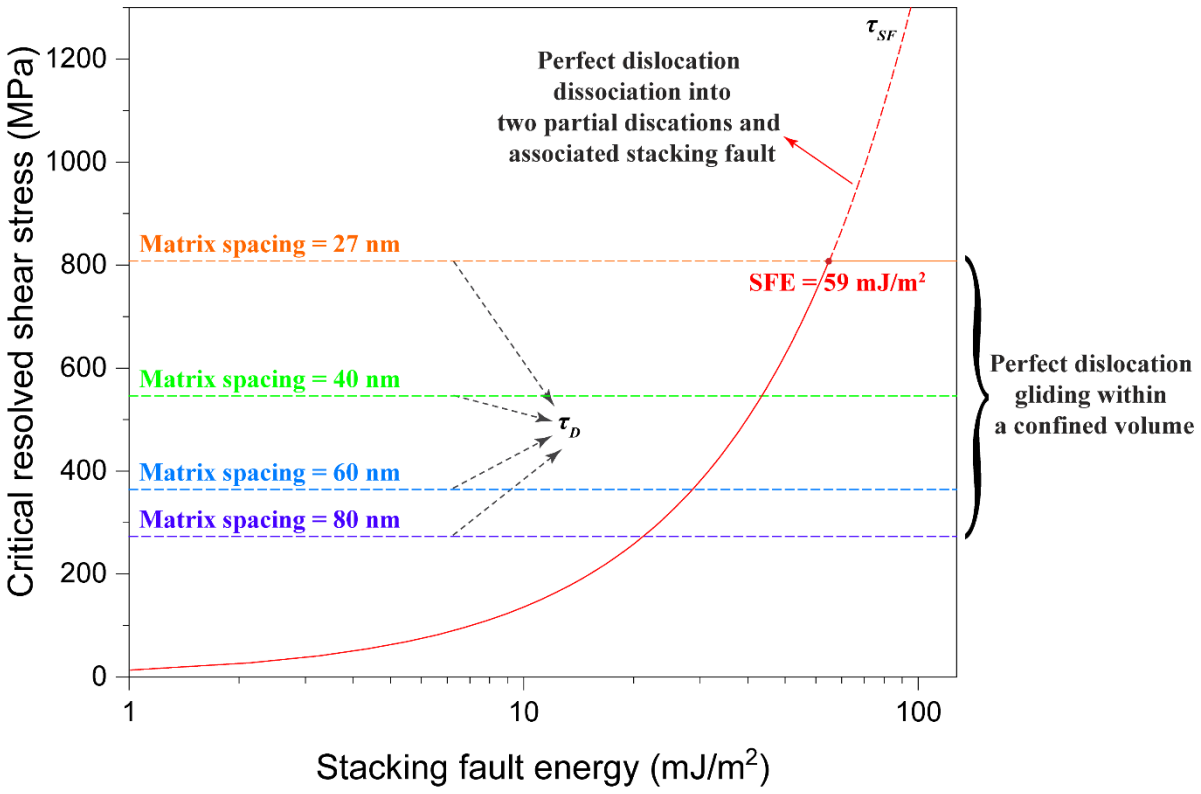

Fig. 14. The critical resolved shear stress required for perfect dislocations gliding through the narrow matrix channels and dissociation into partial dislocations is plotted as a function of the stacking fault energy of the matrix phase. Various matrix spacings are considered in this plot to reveal the extra resistance from the geometric constraint to the movement of dislocations.

Figure 14 shows the critical resolved shear stress for perfect dislocation gliding (τ_D) and dissociation (τ_{SF}) as a function of the stacking fault energy of the matrix phase. As we can see, the critical resolved shear stress for the initiation of stacking fault (τ_{SF}) increases as the stacking fault energy increases. In contrast, the critical resolved shear stress for dislocation gliding (τ_D) remains constant with respect to varied stacking fault energies. As evident in **Fig. 9**, the stacking faults act as the main plasticity carriers among the 30Ni2Ti2Ta alloy, which suggests that the critical shear stress for dislocation dissociation is lower than that of spatially confined dislocation gliding. As illustrated in **Fig. 14**, dislocation dissociation are favorable when the stacking fault energy is lower than 59 mJ/m^2 with respect to dislocation gliding within

a matrix spacing of ~ 27 nm. In fact, a low-stacking-fault-energy matrix is expected for the current 30Ni2Ti2Ta alloy due to the concentrated Co content in the matrix phase (as high as ~ 80 at.% according to the atom probe analyses). For instance, the stacking fault energy is around 20 - 30 mJ/m^2 for a Ni-based superalloy AM-3 with a matrix composition of Ni-12Co-27.2Cr-3.4Al-0.4Ti-0.4Ta-2.9Mo-1.5W (at.%) [69]. As compared with Ni-based superalloys, the Co-rich matrix tends to retain a lower stacking fault energy and promote the dissociation of perfect dislocation and associated stacking fault formation upon plastically deformed. In addition, previous studies indicated that superalloys with a low stacking fault energy matrix demonstrate a superior creep resistance by facilitating the formation of high-density stacking faults, which act as additional barriers to the movement of the matrix dislocation [70]. Therefore, further creep property investigation would be of interest for Co-rich alloys with a low stacking fault energy matrix.

Moreover, it should also be noted that the narrow matrix channel width also plays a vital role in facilitating stacking fault formation. Additionally, we calculated the critical shear stress values for dislocation gliding within a matrix spacing of 40, 60, and 80 nm in **Fig. 14**. The critical resolved shear stress for perfect dislocations gliding is substantially reduced once the geometric constraint (matrix channel width) is partially eased (widened). Under such circumstances, the stacking fault formation might not be favorable even with a low stacking fault energy matrix. The high concentrations of the γ′-stabilizing elements (e.g., Al, Nb, Ti, and Ta) elevate the volume fraction of the γ′ precipitates, providing a pronounced microstructure refinement effect and dividing the γ phase into well-defined matrix channels. In addition, the fully coherent γ/γ′ interfaces also decrease the nucleation barrier for γ′ precipitation, thus contributing to the high number density of the precipitates. The joint characteristics of the high volume fraction together with the high number density of the precipitates result in the narrow matrix channels, which in turn facilitates the stacking fault formation upon plastic deformation.

4.4. The multicomponent γ′ precipitates with high planar fault energies

The dislocation-precipitate interaction can be divided into two primary categories: The Orowan looping mechanism and the particle shearing mechanism. It should be noted that, due to the geometric confinement of the narrow matrix channels, the formation of loops around a single particle is unfavorable since dislocation motion through high-density precipitates rarely occurs [62]. However, particle shearing events are also absent from our room-temperature plastically deformed specimens: the propagation of stacking faults via Shockey partial dislocation is blocked at the γ/γ′ interfaces without entering the γ′ precipitates. Particle shearing requires the matrix dislocations to cut into the ordered $L1_2$ precipitates. Associated planar faults will be generated during particle shearing, the type of which depends on the involved Burgers vectors of the sheared dislocation. An anti-phase boundary (APB) would be created if dislocation with a Burger vector of a/2<110> shear into the $L1_2$ particle, during which the shear stress should be high enough to overcome the APB energy since the formation of APB disrupts the chemical ordering between neighboring atom species [71]. Likewise, a Kear partial dislocation with a Burgers vector of a/3<112> shearing into the γ′ precipitates creates a SISF in the ordered $L1_2$ structure [72]. The onset of SISF shearing also requires the critical shear stress to overcome the energy barrier, that is, SISF energy in this case. In the current study, we did not observe a particle shearing event which usually involves APB-coupled dislocation pairs or superlattice stacking faults within the room-temperature deformed substructures. The absence of the particle shearing, either APB or SISF shearing, should ascribed to the high APB energy and SISF energy that the shear stress exerts on the matrix dislocations are not enough to push the matrix dislocations into the ordered $L1_2$ precipitates.

To rationalize the absence of the particle shearing events upon the plastic deformation at ambient temperature, the effect of alloying additions on the planar fault energies of the precipitates in the 30Ni2Ti2Ta alloy is discussed here. It should be noted that the precipitation

is highly alloyed, and its composition is distinctively different from that of the compositional simple counterpart (e.g., $Co_3(Al, W)$ and Ni_3Al phase) in the following two aspects. First, the γ′ precipitates are stabilized by substantial Ni addition (~ 35 at.% according to the APT analyses); therefore, the Co sublattice sites are partially substituted by Ni in the $L1_2$ structure. Second, considerable Al sublattice sites have been occupied by Nb, Ti, and Ta atoms in the γ′ phase, whose presences are believed to influence both APB and SISF energies profoundly.

Herein, we calculate the planar fault energies of the multicomponent γ′ precipitates by first-principle calculations to highlight the strengthening contribution to the $L1_2$ precipitates through multiple alloying additions. A supercell composed of six-layers of {111} plane with and without planar faults was constructed for the planar fault energy calculations. The thermodynamic cost of forming a planar fault is quantified by:

$$\gamma_{\mathrm{i}} = (E_{\mathrm{faulted}} - E_{\mathrm{perfect}})/A_{\mathrm{i}} \quad (7)$$

where γ_{i} is the planar fault energy, i represents APB or SISF, E_{faulted} and E_{perfect} are the energy of the structure with and without planar defects, respectively. A_{i} is the area of the slip plane.

Table 3 Planar fault energies of the $L1_2$-type intermetallic compounds. The lattice parameter, Curie temperature, and magnetic state are also shown here.

	Lattice parameter (Å)	Curie temperature T_C (K)	Magnetic state	γ_{APB} (mJ/m^2)	γ_{SISF} (mJ/m^2)
Ni_3Al	3.572	33	PM	240	104
Co_3Al	3.582	6	PM	96	-114
$(Co_{40}Ni_{35})Al_{25}$	3.579	326	FM	218	83
$(Co_{40}Ni_{35})(Al_{13}Ti_3Ta_3Nb_6)$	3.616	130	PM	530	286

As shown in **Table 3**, the calculated planar fault energies of the Ni_3Al phase are in well agreement with previous studies, e.g., Myrasov et al. [73] (an APB energy of 210 mJ/m^2 and a

SISF energy of 80 mJ/m^2) and Schoeck et al. [74] (an APB energy of 220 mJ/m^2 and a SISF energy of 79 mJ/m^2). A negative SISF energy value of the Co_3Al phase suggests that this structure is unstable upon dislocation shearing. The partial substitution of Co with Ni stabilized the Co_3Al phase by tuning the SISF energy into a positive value with a simultaneously elevated APB energy in the $(Co_{40}Ni_{35})Al_{25}$ phase (**Table 3**). More surprisingly, the sublattice Al site occupation of Nb, Ti, and Ta elements further increased both the APB and SISF energy considerably, reaching 530 mJ/m^2 and 286 mJ/m^2, respectively. Therefore, the current multicomponent γ′ precipitates possess both ultrahigh APB and SISF energies, which markedly increase the shearing resistance towards matrix dislocations. In this way, the propagation of the dissociated matrix dislocation got stopped at the γ/γ′ interfaces (**Fig. 9**), together with an absent APB-based particle shearing in the present 30Ni2Ti2Ta alloy upon plastic deformation at ambient temperature.

4.5. The origin of yield anomaly

In contrast with the fact that partial dislocations cannot penetrate the γ′ precipitates at room temperature, the SSF-based γ′ particle shearing was activated at 700 °C. The density-functional theory predicts that the SISF energy is negatively correlated to the temperature in the $L1_2$-$(Co, Ni)_3Al$ structure [75]. Therefore, the activation of SSF-based particle shearing can be possibly ascribed to the decreased SISF energy at elevated deformation temperatures.

From a traditional perspective, the onset of anomalous yield behavior can be attributed to the thermally-assisted cross-slip of the screw segments of the APB-coupled superpartial dislocations from {111} to {100} planes, resulting in the formation of Kear-Wilsdorf locks in commercial Ni-based superalloys [62, 76]. Instead of particle shearing via APB-coupled dislocation pairs and associated cross-slip events, we observed high-density SSF-shearing at the peak temperature in the present study (**Fig. 10**). Stacking fault interfaces formed in the wake of the gliding of a leading partial dislocation, which act as obstacles for the subsequent

partial dislocation shearing through [77]. In addition, the interactions between SSFs resulted in sessile stair-rod dislocation configurations, preventing further expansion of the stacking fault [78]. Therefore, the yield anomaly can be rationalized by dense SSF interactions and the associated hardening effect in the $L1_2$ particles. Similar SSF-shearing events have been observed in the Co-Ti-Cr alloy upon high-temperature compressions, which also result in the yield anomaly [79]. It should be noted that SSF-shearing has only been activated in the Co-Al-W-Ta alloy at temperatures above the peak temperature, which allows the Co-Al-W-Ta alloy to retain most of its strength at this temperature region [40]. Therefore, a more detailed understanding towards the unique SSF-based particle shearing is worthy of the investigation, and further to enhance the temperature capabilities of Co-rich high-temperature alloys.

5. Conclusion

In this study, we demonstrated the feasibility of designing novel high-temperature structural materials within the multicomponent Co-Al-Nb-based alloy systems. The present findings can be summarized by the following points:

1) We highlight the formation of the $L1_2$-Co_3(Al, Nb) precipitates in equilibrium with the γ-Co matrix and the B2-CoAl phase at 700 °C in the ternary Co-10Al-3Nb alloy. Both Al and Nb are preferentially partitioned to the $L1_2$ precipitates and contribute to the enhanced phase stability. Unfortunately, the $L1_2$ phase transformed into the Laves phase as the aging temperature increased to 800 °C, indicating insufficient thermal stability of this type of $L1_2$ precipitates in the ternary Co-Al-Nb alloy system.
2) Several alloying additions were identified to be beneficial for the microstructural stability in the baseline Co-Al-Nb alloys. Alloying addition of Ni was found to suppress the formation of the B2 phase, resulting in a clean γ′-γ dual-phase microstructure without inducing brittle intermetallic phase formation. Ti and Ta were identified as potent γ′-

stabilizing elements by strongly partitioning to the γ′ precipitates. These elements substantially enhanced the thermal stability of the $L1_2$ precipitates and increased the γ′-solvus temperature to 1150 °C in the modified Co-Al-Nb-based alloys. These experimental results on the thermal stability of the $L1_2$-Co_3(Al, Nb) phase and alloying effects among the Co-Al-Nb-based alloys are in good agreement with first-principle calculations and thermodynamic calculations.

3) The newly developed multicomponent Co-rich alloy exhibited superior strengths at both ambient and elevated temperatures, reaching 1023 ± 27 MPa at 25 °C and 897 ± 53 MPa at 700 °C, respectively. The strength of the Co-rich alloy is even superior to the commercial Ni-based superalloy Waspaloy over the entire temperature range. Noticeably, nanoscale stacking faults were geometrically confined in the matrix channels upon deformation at ambient temperature and acted as the primary plasticity carriers. The low stacking fault energy matrix and the narrow matrix channel are expected to promote the formation of the high-density stacking fault in the matrix channels. The absence of particle shearing at ambient temperature is attributed to the ultrahigh planar fault energies of the multicomponent γ′ precipitates and the resultant high shearing resistance towards matrix dislocations. The activation of superlattice-stacking-fault-based particle shearing has been observed after strained at 700 °C, whose interactions are responsible for the yield anomaly at this temperature.

Declaration of Competing Interest

The authors declare that they have no known competing financial interests or personal relationships that could have appeared to influence the work reported in this paper.

Acknowledgements

The authors from City University of Hong Kong (CityU) are grateful for the financial support from the National Natural Science Foundation of China (Grant 52101151), the CityU Shenzhen Research Institute (SRI) (Grant 2020A1515110647), as well as the Hong Kong Research Grant Council (RGC) with CityU Grant 11213319, 11202718, 21205621, 9610498. The author from Xiamen University is grateful for the Youth Innovation Fund Project of Xiamen (Grant No. 3502Z20206057). The authors from Hong Kong Polytechnic University are grateful for the financial support from National Natural Science Foundation of China (No. 51801169 and 52171162) and HK Research Grants Council (ECS 25202719 and GRF 15227121).

References

[1] J. Sato, T. Omori, K. Oikawa, I. Ohnuma, R. Kainuma, K. Ishida, Cobalt-base high-temperature alloys, Science 312 (2006) 90-91.

[2] E.A. Lass, M.E. Williams, C.E. Campbell, K.-W. Moon, U.R. Kattner, γ′ phase stability and phase equilibrium in ternary Co-Al-W at 900 °C, J. Phase Equilibria Diffus. 35 (2014) 711-723.

[3] J.E. Saal, C. Wolverton, Thermodynamic stability of Co-Al-W $L1_2$ γ′, Acta Mater. 61 (2013) 2330-2338.

[4] Y. Tsukamoto, S. Kobayashi, T. Takasugi, The stability of γ′-Co_3(Al, W) phase in Co-Al-W ternary system, Mater. Sci. Forum, 2010, pp. 448-451.

[5] C.T. Sims, N.S. Stoloff, W.C. Hagel, Superalloys II, Wiley New York1987.

[6] B. Cao, T. Yang, W.H. Liu, C.T. Liu, Precipitation-hardened high-entropy alloys for high-temperature applications: A critical review, MRS Bull. 44 (2019) 854-859.

[7] T. Omori, K. Oikawa, J. Sato, I. Ohnuma, U.R. Kattner, R. Kainuma, K. Ishida, Partition behavior of alloying elements and phase transformation temperatures in Co-Al-W-base quaternary systems, Intermetallics 32 (2013) 274-283.

[8] B. Cao, T. Yang, L. Fan, J. Luan, Z. Jiao, C.T. Liu, Refractory alloying additions on the thermal stability and mechanical properties of high-entropy alloys, Mater. Sci. Eng. A (2020) 140020.

[9] M. Pröbstle, S. Neumeier, P. Feldner, R. Rettig, H. Helmer, R. Singer, M. Göken, Improved creep strength of nickel-base superalloys by optimized γ/γ′ partitioning behavior of solid solution strengthening elements, Mater. Sci. Eng. A 676 (2016) 411-420.

[10] E. Fleischmann, M.K. Miller, E. Affeldt, U. Glatzel, Quantitative experimental determination of the solid solution hardening potential of rhenium, tungsten and molybdenum in single-crystal nickel-based superalloys, Acta Mater. 87 (2015) 350-356.

[11] C.K. Sudbrack, T.D. Ziebell, R.D. Noebe, D.N. Seidman, Effects of a tungsten addition on the morphological evolution, spatial correlations and temporal evolution of a model Ni-Al-Cr superalloy, Acta Mater. 56 (2008) 448-463.

[12] C. Booth-Morrison, R.D. Noebe, D.N. Seidman, Effects of tantalum on the temporal evolution of a model Ni-Al-Cr superalloy during phase decomposition, Acta Mater. 57 (2009) 909-920.

[13] T. Omori, Y. Sutou, K. Oikawa, R. Kainuma, K. Ishida, Shape memory and magnetic properties of Co-Al ferromagnetic shape memory alloys, Mater. Sci. Eng. A 438-440 (2006) 1045-1049.

[14] W. Xu, S. Shang, C. Wang, T. Gang, Y. Huang, L. Chen, X. Liu, Z. Liu, Accelerating exploitation of Co-Al-based superalloys from theoretical study, Mater. Des. 142 (2018) 139-148.

[15] C. Jiang, First-principles study of Co_3(Al, W) alloys using special quasi-random structures, Scripta Mater. 59 (2008) 1075-1078.

[16] W.W. Xu, Z.Y. Xiong, X.G. Gong, G.H. Yin, L.J. Chen, C.P. Wang, X.J. Liu, Accelerating the discovery of novel γ/γ' Co-based superalloys by probing temperature and alloying effects on the γ' precipitates, Materialia 18 (2021) 101171.

[17] M. Jin, N. Miao, W. Zhao, J. Zhou, Q. Du, Z. Sun, Structural stability and mechanical properties of Co_3(Al, M) (M = Ti, V, Cr, Zr, Nb, Mo, Hf, Ta, W) compounds, Comp. Mater. Sci. 148 (2018) 27-37.

[18] S. Makineni, B. Nithin, K. Chattopadhyay, A new tungsten-free γ-γ′ Co-Al-Mo-Nb-based superalloy, Scripta Mater. 98 (2015) 36-39.

[19] F.L.R. Tirado, J.P. Toinin, D.C. Dunand, γ + γ′ microstructures in the Co-Ta-V and Co-Nb-V ternary systems, Acta Mater. 151 (2018) 137-148.

[20] V. Kokorin, K. Chuistov, Initial stages of decomposition of supersaturated solid solutions Co-Ta and Co-Nb, Fiz. Metallov. Metalloved. 21 (1966) 311-314.
[21] P.E. Blöchl, Projector augmented-wave method, Phys. Rev. B 50 (1994) 17953.
[22] G. Kresse, J. Furthmüller, Efficient iterative schemes for ab initio total-energy calculations using a plane-wave basis set, Phys. Rev. B 54 (1996) 11169.
[23] J.P. Perdew, K. Burke, M. Ernzerhof, Generalized gradient approximation made simple, Phys. Rev. Lett. 77 (1996) 3865.
[24] H.J. Monkhorst, J.D. Pack, Special points for Brillouin-zone integrations, Phys. Rev. B 13 (1976) 5188.
[25] O. Andersen, O. Jepsen, G. Krier, Exact muffin-tin orbital theory, Lect. Meth. of Electron. Struct. Calc. (1994) 63-124.
[26] L. Vitos, Computational quantum mechanics for materials engineers: the EMTO method and applications, Springer Science & Business Media2007.
[27] P. Soven, Coherent-potential model of substitutional disordered alloys, Phys. Rev. 156 (1967) 809.
[28] B. Gyorffy, Coherent-potential approximation for a nonoverlapping-muffin-tin-potential model of random substitutional alloys, Phys. Rev. B 5 (1972) 2382.
[29] D. Ma, B. Grabowski, F. Körmann, J. Neugebauer, D. Raabe, Ab initio thermodynamics of the CoCrFeMnNi high entropy alloy: Importance of entropy contributions beyond the configurational one, Acta Mater. 100 (2015) 90-97.
[30] B. Gyorffy, A. Pindor, J. Staunton, G. Stocks, H. Winter, A first-principles theory of ferromagnetic phase transitions in metals, J. Phys. F: Met. Phys. 15 (1985) 1337.
[31] D. Collins, L. Yan, E. Marquis, L. Connor, J. Ciardiello, A. Evans, H. Stone, Lattice misfit during ageing of a polycrystalline nickel-base superalloy, Acta Mater. 61 (2013) 7791-7804.
[32] P. Viatour, J. Drapier, D. Coutsouradis, Stability of the gamma prime Co_3Ti compound in simple and complex Co alloys, Cobalt (1973) 67-74.
[33] C. Zenk, S. Neumeier, H. Stone, M. Göken, Mechanical properties and lattice misfit of γ/γ′ strengthened Co-base superalloys in the Co-W-Al-Ti quaternary system, Intermetallics 55 (2014) 28-39.
[34] C. He, F. Stein, M. Palm, Thermodynamic description of the systems Co-Nb, Al-Nb and Co-Al-Nb, J. Alloys Compd. 637 (2015) 361-375.
[35] O. Dovbenko, F. Stein, M. Palm, O. Prymak, Experimental determination of the ternary Co-Al-Nb phase diagram, Intermetallics 18 (2010) 2191-2207.
[36] L. Zhu, C. Wei, H. Qi, L. Jiang, Z. Jin, J.-C. Zhao, Experimental investigation of phase equilibria in the Co-rich part of the Co-Al-X (X= W, Mo, Nb, Ni, Ta) ternary systems using diffusion multiples, J. Alloys Compd. 691 (2017) 110-118.
[37] Y. Chen, C. Wang, J. Ruan, T. Omori, R. Kainuma, K. Ishida, X. Liu, High-strength Co-Al-V-base superalloys strengthened by γ′-Co_3(Al, V) with high solvus temperature, Acta Mater. 170 (2019) 62-74.
[38] K. Shinagawa, T. Omori, J. Sato, K. Oikawa, I. Ohnuma, R. Kainuma, K. Ishida, Phase equilibria and microstructure on γ′ phase in Co-Ni-Al-W system, Mater. Trans. 49 (2008) 1474-1479.
[39] F. Xue, H. Zhou, Q. Shi, X. Chen, H. Chang, M. Wang, Q. Feng, Creep behavior in a γ′ strengthened Co–Al–W–Ta–Ti single-crystal alloy at 1000 °C, Scripta Mater. 97 (2015) 37-40.
[40] A. Suzuki, T.M. Pollock, High-temperature strength and deformation of γ/γ′ two-phase Co-Al-W-base alloys, Acta Mater. 56 (2008) 1288-1297.
[41] P.J. Bocchini, C.K. Sudbrack, R.D. Noebe, D.C. Dunand, D.N. Seidman, Effects of titanium substitutions for aluminum and tungsten in Co-10Ni-9Al-9W (at%) superalloys, Mater. Sci. Eng. A 705 (2017) 122-132.

[42] H.-Y. Yan, V. Vorontsov, D. Dye, Alloying effects in polycrystalline γ′ strengthened Co-Al-W base alloys, Intermetallics 48 (2014) 44-53.
[43] F. Stein, D. Jiang, M. Palm, G. Sauthoff, D. Grüner, G. Kreiner, Experimental reinvestigation of the Co-Nb phase diagram, Intermetallics 16 (2008) 785-792.
[44] A. Mottura, A. Janotti, T.M. Pollock, Alloying Effects in the γ′ Phase of Co-Based Superalloys, Proc. 12 Int. Symp. Superalloys, TMS, 2012, pp. 685-693.
[45] L. Feng, D. Lv, R. Rhein, J. Goiri, M. Titus, A. Van der Ven, T. Pollock, Y. Wang, Shearing of γ'particles in Co-base and Co-Ni-base superalloys, Acta Mater. 161 (2018) 99-109.
[46] Y. Chen, C. Wang, J. Ruan, S. Yang, T. Omori, R. Kainuma, K. Ishida, J. Han, Y. Lu, X. Liu, Development of low-density γ/γ′ Co-Al-Ta-based superalloys with high solvus temperature, Acta Mater. (2020).
[47] S. Meher, R. Banerjee, Partitioning and site occupancy of Ta and Mo in Co-base γ/γ′ alloys studied by atom probe tomography, Intermetallics 49 (2014) 138-142.
[48] P. Pandey, S.K. Makineni, A. Samanta, A. Sharma, S.M. Das, B. Nithin, C. Srivastava, A.K. Singh, D. Raabe, B. Gault, Elemental site occupancy in the $L1_2$ A_3B ordered intermetallic phase in Co-based superalloys and its influence on the microstructure, Acta Mater. 163 (2019) 140-153.
[49] L.P. Freund, A. Stark, F. Pyczak, N. Schell, M. Göken, S. Neumeier, The grain boundary pinning effect of the μ phase in an advanced polycrystalline γ/γ′ Co-base superalloy, J. Alloys Compd. 753 (2018) 333-342.
[50] C. Nickel, ASM Specialty Handbook, ASM International Materials Park, OH (2000) 44073-0002.
[51] C.H. Zenk, I. Povstugar, R. Li, F. Rinaldi, S. Neumeier, D. Raabe, M. Göken, A novel type of Co-Ti-Cr-base γ/γ′ superalloys with low mass density, Acta Mater. 135 (2017) 244-251.
[52] A. Suzuki, G.C. DeNolf, T.M. Pollock, Flow stress anomalies in γ/γ′ two-phase Co-Al-W-base alloys, Scr. Mater. 56 (2007) 385-388.
[53] T. Pollock, A. Argon, Creep resistance of CMSX-3 nickel base superalloy single crystals, Acta Metall. Mater. 40 (1992) 1-30.
[54] M.S. Titus, Y.M. Eggeler, A. Suzuki, T.M. Pollock, Creep-induced planar defects in $L1_2$-containing Co-and CoNi-base single-crystal superalloys, Acta Mater. 82 (2015) 530-539.
[55] Y. Eggeler, J. Müller, M. Titus, A. Suzuki, T. Pollock, E. Spiecker, Planar defect formation in the γ′ phase during high temperature creep in single crystal CoNi-base superalloys, Acta Mater. 113 (2016) 335-349.
[56] S. Makineni, B. Nithin, K. Chattopadhyay, Synthesis of a new tungsten-free γ-γ′ cobalt-based superalloy by tuning alloying additions, Acta Mater. 85 (2015) 85-94.
[57] S. Makineni, A. Samanta, T. Rojhirunsakool, T. Alam, B. Nithin, A. Singh, R. Banerjee, K. Chattopadhyay, A new class of high strength high temperature Cobalt based γ-γ′ Co-Mo-Al alloys stabilized with Ta addition, Acta Mater. 97 (2015) 29-40.
[58] H.J. Im, S.K. Makineni, B. Gault, F. Stein, D. Raabe, P.-P. Choi, Elemental partitioning and site-occupancy in γ/γ′ forming Co-Ti-Mo and Co-Ti-Cr alloys, Scripta Mater. 154 (2018) 159-162.
[59] Z. Liang, M. Göken, U. Lorenz, S. Neumeier, M. Oehring, F. Pyczak, A. Stark, L. Wang, Influence of small amounts of Si and Cr on the high temperature oxidation behavior of novel cobalt base superalloys, Corros. Sci. 184 (2021) 109388.
[60] B. Cao, Y. Zhao, T. Yang, C.T. Liu, $L1_2$-Strengthened Co-Rich Alloys for High-Temperature Structural Applications: A Critical Review, Adv. Eng. Mater. 23 (2021) 2100453.

[61] B. Decamps, S. Raujol, A. Coujou, F. Pettinari-Sturmel, N. Clement, D. Locq, P. Caron, On the shearing mechanism of γ′ precipitates by a single (a/6)⟨112⟩ Shockley partial in Ni-based superalloys, Philos. Mag. 84 (2004) 91-107.
[62] T. Pollock, R. Field, Dislocations and high-temperature plastic deformation of superalloy single crystals, Dislocations in solids, Elsevier 2002, pp. 547-618.
[63] G. Saunders, D. Ball, M. Cankurtaran, Q. Wang, E. Arnscheidt, C. Jacobs, F. Imbierwitz, J. Pelzl, H. Bach, Ultrasonic study of the temperature and pressure dependences of the elastic propertiesof fcc Co-Mn alloy single crystals, Phys. Rev. B 55 (1997) 11181.
[64] W. Voigt, Ueber die Beziehung zwischen den beiden Elasticitätsconstanten isotroper Körper, Ann Phys. 274 (1889) 573-587.
[65] A. Reuß, Berechnung der fließgrenze von mischkristallen auf grund der plastizitätsbedingung für einkristalle, Z. Angew. Math. Mech. 9 (1929) 49-58.
[66] R. Hill, The elastic behaviour of a crystalline aggregate, Proc. Phys. Soc. A 65 (1952) 349.
[67] G.I. Taylor, H. Quinney, The plastic distortion of metals, Philos. Trans. Royal Soc. A, 230 (1931) 323-362.
[68] T. Byun, On the stress dependence of partial dislocation separation and deformation microstructure in austenitic stainless steels, Acta Mater. 51 (2003) 3063-3071.
[69] F. Diologent, P. Caron, On the creep behavior at 1033 K of new generation single-crystal superalloys, Mater. Sci. Eng. A 385 (2004) 245-257.
[70] S. Ma, L. Carroll, T. Pollock, Development of γ phase stacking faults during high temperature creep of Ru-containing single crystal superalloys, Acta Mater. 55 (2007) 5802-5812.
[71] P. Beauchamp, J. Douin, P. Veyssière, Dependence of the antiphase boundary energy upon orientation in the $L1_2$ structure, Philos. Mag. A 55 (1987) 565-581.
[72] W.W. Milligan, S.D. Antolovich, The mechanisms and temperature dependence of superlattice stacking fault formation in the single-crystal superalloy PWA 1480, Metall. Trans. A 22 (1991) 2309-2318.
[73] O. Mryasov, Y.N. Gornostyrev, M. Van Schilfgaarde, A. Freeman, Superdislocation core structure in $L1_2$ Ni_3Al, Ni_3Ge and Fe_3Ge: Peierls–Nabarro analysis starting from ab-initio GSF energetics calculations, Acta Mater. 50 (2002) 4545-4554.
[74] G. Schoeck, S. Kohlhammer, M. Fahnle, Planar dissociations and recombination energy of [110] superdislocations in Ni_3Al: Generalized Peierls model in combination with ab initio electron theory, Philos. Mag. Lett. 79 (1999) 849-857.
[75] A. Breidi, J. Allen, A. Mottura, First-principles modeling of superlattice intrinsic stacking fault energies in Ni3Al based alloys, Acta Mater. 145 (2018) 97-108.
[76] B. Kear, Dislocation configurations and work hardening in Cu_3Au crystals, Acta Metall. 12 (1964) 555-569.
[77] S. Lu, S. Antonov, L. Li, C. Liu, X. Zhang, Y. Zheng, H.L. Fraser, Q. Feng, Atomic structure and elemental segregation behavior of creep defects in a Co-Al-W-based single crystal superalloys under high temperature and low stress, Acta Mater. 190 (2020) 16-28.
[78] Q.-J. Li, J. Li, Z.-W. Shan, E. Ma, Strongly correlated breeding of high-speed dislocations, Acta Mater. 119 (2016) 229-241.
[79] A. Bezold, N. Volz, M. Lenz, C. Zenk, E. Spiecker, M. Mills, M. Göken, S. Neumeier, Yielding behavior of a single-crystalline γ'-strengthened Co-Ti-Cr superalloy, Scr. Mater. 200 (2021) 113928.

Supplementary data

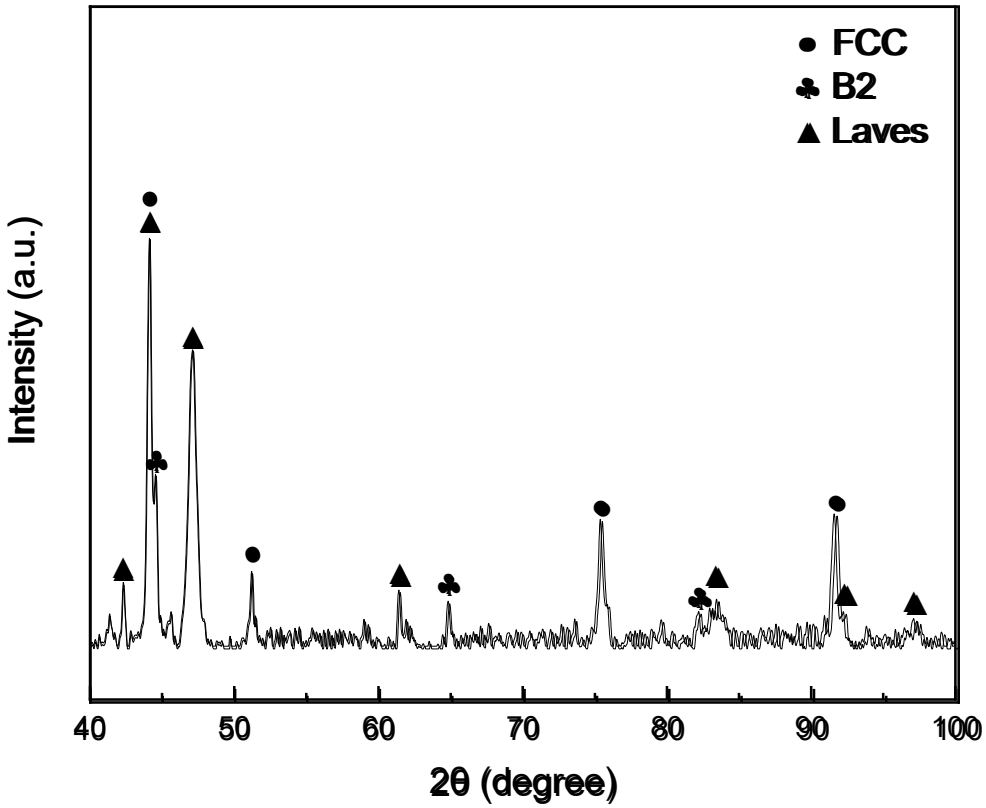

Fig. S1. (a) X-ray diffraction pattern of the ternary Co-10Al-3Nb alloy aged at 800 °C for 336 h.

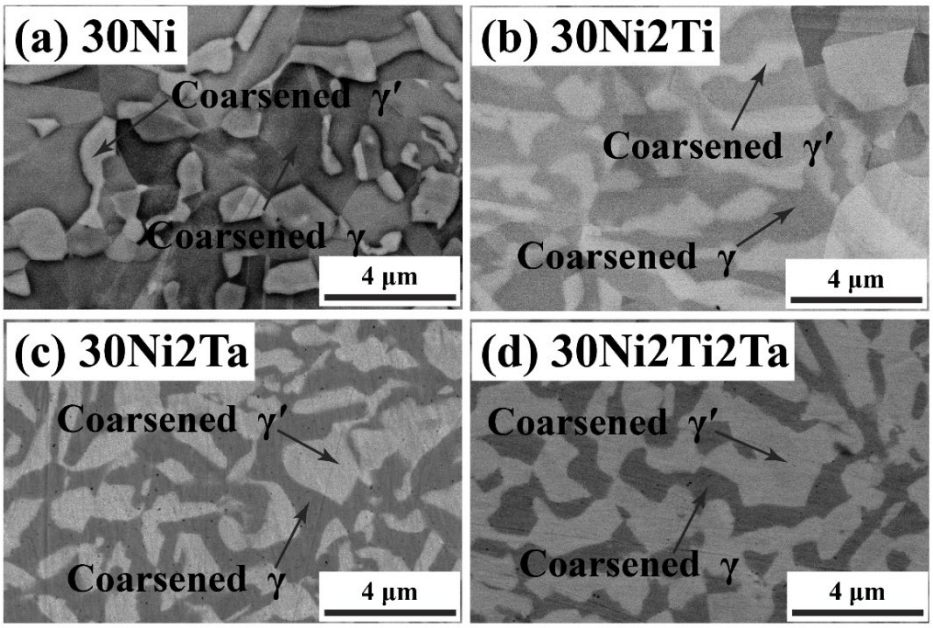

Fig. S2. Back-scattered electron micrographs of the Co-based alloys subjected to aging at 800 °C for 168 h followed by cold-rolled with 50% reduction in thickness: (a) Co-10Al-3Nb-30Ni (30Ni) alloy, (b) Co-10Al-3Nb-30Ni-2Ti (30Ni2Ti) alloy, (c) Co-10Al-3Nb-30Ni-2Ta (30Ni2Ta) alloy, and (d) Co-10Al-3Nb-30Ni-2Ti-2Ta (30Ni2Ti2Ta) alloy.

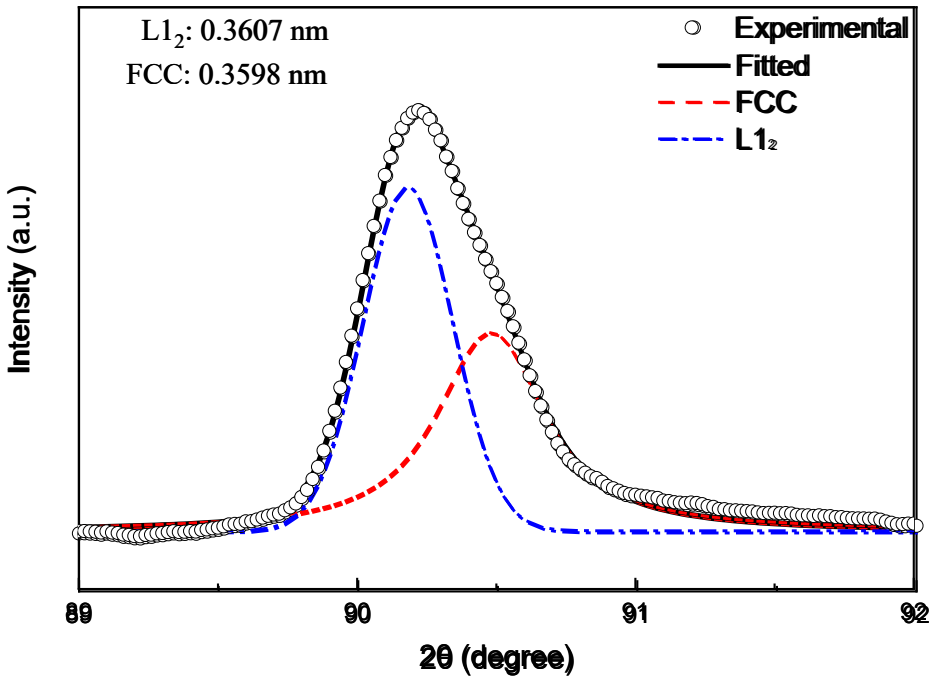

Fig. S3. X-ray diffraction pattern and associated peak deconvolution of the aged 30Ni2Ti2Ta alloy. The lattice parameters of the γ′ and γ phases are calculated via the peak deconvolution obtained from the (311) plane.